CHALMERS
UNIVERSITY OF TECHNOLOGY

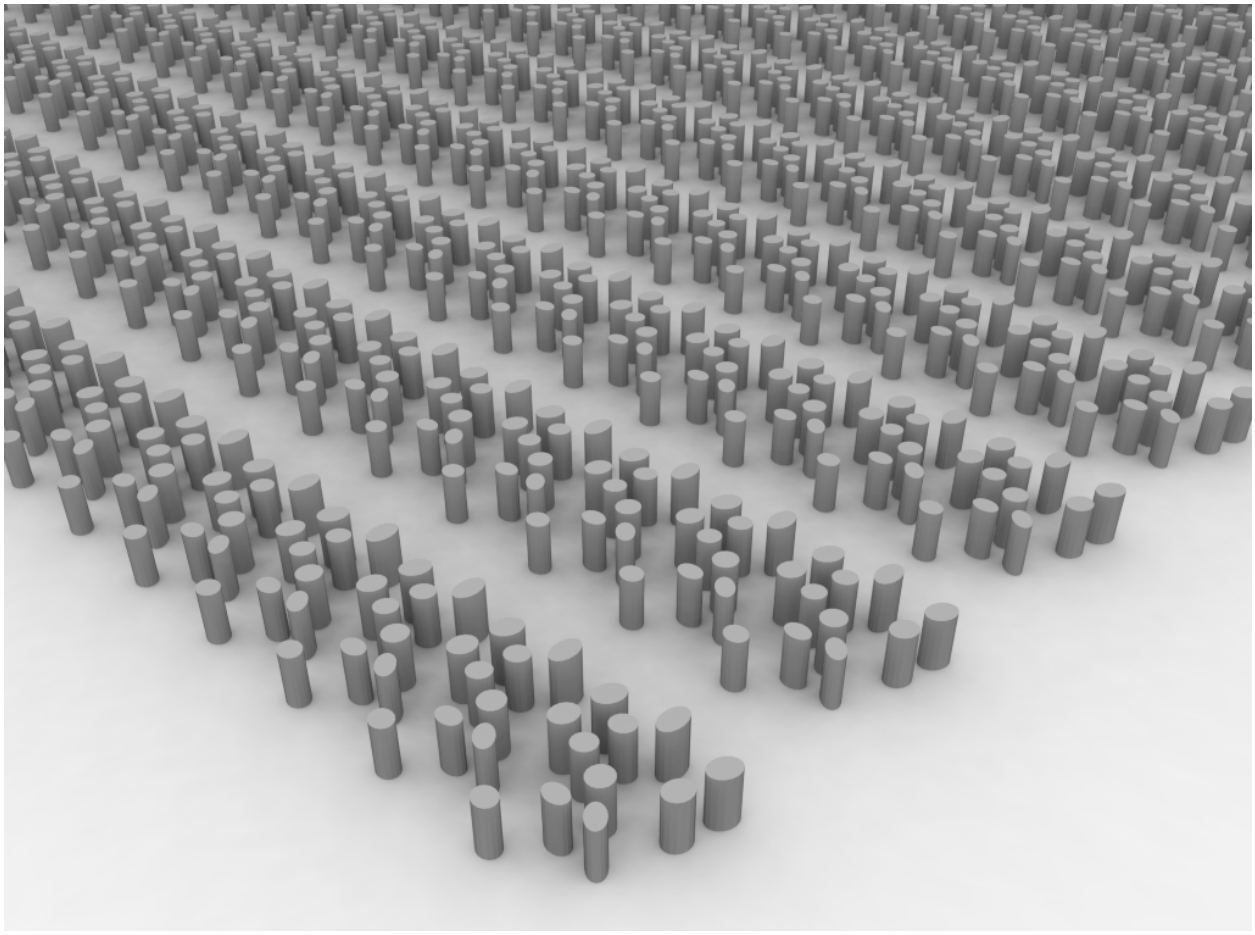

Global optimization of optical metasurfaces using the RCWA method

Master's thesis in Physics

LUDWIG SCHERQVIST HALLDNER

DEPARTMENT OF PHYSICS

CHALMERS UNIVERSITY OF TECHNOLOGY
Gothenburg, Sweden 2023
www.chalmers.se

Master's thesis 2023

Global optimization of optical metasurfaces using the RCWA method

LUDWIG SCHERQVIST HALLDNER

CHALMERS
UNIVERSITY OF TECHNOLOGY

Department of Physics
Division of Nano and Biophysics
Chalmers University of Technology
Gothenburg, Sweden 2023

Global optimization of optical metasurfaces using the RCWA method
LUDWIG SCHERQVIST HALLDNER

Supervisors: Mikael Käll, Department of Physics
Mindaugas Juodenas, Department of Physics
Vasilii Mylnikov, Department of Physics
Examiner: Mikael Käll, Department of Physics

Master's Thesis 2023
Department of Physics
Division of Nano and Biophysics
Chalmers University of Technology
SE-412 96 Gothenburg
Telephone +46 31 772 1000

Cover: A rendered 3D figure of the 30° grating from figure 4.12 viewed from the lower left corner of the metasurface. For scale, the periodicities of the grating is 950 nm in the short direction and 2128 nm in the long direction. The substrate (colored white in this figure) is made of SiO_2, while the pillars (colored grey) are made of Si.

Typeset in LaTeX
Printed by Chalmers Reproservice
Gothenburg Sweden 2023

Global optimization of optical metasurfaces using the RCWA method
LUDWIG SCHERQVIST HALLDNER
Department of Physics
Chalmers University of Technology

Abstract

A metaatom is a nanoparticle that interacts with light such that it creates a phase-shift. Through using these metaatoms as building blocks, one may create a metasurface. By simulating a metasurface with the S^4 program, which uses the RCWA (Rigorous Coupled Wave Analysis) method, one may see how well it performs. When optimizing the structure, simulations were done such that the positions, radii and rotation of the elliptical cylinder metaatoms used for the metasurface were varied. It is possible to optimize a grating that bends normal incident light with an angle given by the periodicity of the metasurface in one direction. When slowly varying the periodicity of a metasurface grating (metagrating), it is possible to create multiple metagratings that later may be combined into a lens by combining the metagratings in large rings. These rings are then placed around a center piece, which uses a phase-mapping approach instead. By comparing results with the metasurface lens that J. Byrnes et al. [1] had done, the results are similar. Since they also used the RCWA method, a grating optimized with the FDTD (Finite difference time domain) method by Paniagua-Domínguez et al. [2] was simulated with the S^4 method and compared to their FDTD simulations. The comparison gave a similar overall shape of the polarisation efficiencies, but the RCWA graphs had more noise in them. Through balancing the computational time against the convergence of the efficiencies, 400 vectors for simulations were used in order to optimize three new deflection gratings. The gratings were optimized for deflecting light with a wavelength of 1064 nm in angles of 30°, 45° and 60° in air respectively. These gratings were then fabricated and tested experimentally. The 30° grating did not work as well as in simulations, the 45° grating worked moderately similar, and the 60° grating worked very close to what was expected from simulations. Some more studies would be necessary in order to understand why the simulated efficiencies did not agree with the experimental efficiencies for the 30° grating.

Keywords: metasurface, metaatom, RCWA, metagrating, metalens, S^4

Acknowledgements

I am very grateful for everyone who helped make this project a reality, and supported me during my thesis work. First I would like to thank my examiner Mikael Käll, who helped me formulate the thesis and gave me the possibility to work on this project. Without your helpful inputs this project would not have turned out as well as it did. I would also like to thank my supervisors Mindaugas Juodenas and Vasilii Mylnikov. Thank you for always taking time to answer any questions I had, and making sure that what I expected to do would be realizable. Thank you Mahdi Shanei for constructing the metasurfaces I designed in the clean room and taking the SEM images afterwards. I also want to thank Einstom Engay for setting up the equipment and letting me borrow your lab for measurements. Without your instructions the measurements would not go as smoothly as they did. Next, I would like to thank everyone working in the same part of the floor for making me feel included in different arranged activities. Finally I'd like to thank my family and friends for supporting me through my years of studies.

Ludwig Scherqvist Halldner, Gothenburg, March 2023

Contents

List of Acronyms

Below is a list of acronyms or other technical terms used in this thesis in alphabetical order.

CDL	Conventional Diffractive Lens
FDTD	Finite Difference Time Domain
G-vector	The 2d Fourier components from the surface of the grating
NA	Numerical Aperture
PMW	Plane Monochromatic Wave
RCWA	Rigorous Coupled Wave Analysis
S^4	Stanford Stratified Structure Solver
SEM	Scanning Electron Microscopy
WKB	Wentzel-Kramers-Brillouin
xyrra-list	A list containing information of positions (x,y), half-widths (r_x,r_y) and rotation (a) of all metaatoms in the metagrating referenced

List of Figures

1

Introduction

In optics, the Maxwell equations dictate how light propagates in a material, while the boundary conditions state how the light interacts with a surface. From these equations, it has long been known that one may bend light by letting it pass through a surface at an angle, due to the change in refractive index between the materials. By this knowledge, many optical components have been made. One example of this is an ordinary focusing lens, which uses Snell's law in order to bend collimated light into a focusing point.

Refraction of light passing through an interface between isotropic media is governed by Snell's law. Multiple designs of optical components have been manufactured using this as a basis. For conventional components, it is possible to relate this phenomenon by an equivalent form, where the thickness of the component depends on where the light hits it. This comes from the fact that wave vectors depend on the refractive index, and therefore the propagation in a transparent medium changes the phase by $\Delta\phi = \mathbf{k} \cdot \mathbf{r} = 2\pi n\delta/\lambda_0$, where n is the refractive index in the medium, δ is the thickness of the component in the propagation direction and λ_0 is the wavelength of light in vacuum. The phase shift in turn becomes the difference between the phase propagation in the surrounding medium and in the medium inside the optical component.

Since the phase of the electromagnetic field can be represented as the argument of a complex number, the addition of a phase shift that is 2π large will make no difference on the fields. Therefore, one could create a conventional diffractive lens (CDL), which uses the phase principle in order to make the lens thinner. This is done in such a way that the thickness of the lens becomes around 1 µm [3] (not including the substrate that the lens is situated on). This thickness can be calculated as it is the propagation distance in the material that will accumulate a total phase-shift of 2π.

One way to describe this process is through the phase of light that goes through the optical component. Assuming that the incoming light is collimated and propagates along the optical axis of the component, we know that the phase does not depend on where the light hits a plane perpendicular to the optical axis. As this light propagates straight through the optical component, the phase of the light will depend on how far the light traveled inside the component. When the phase shift over the

surface is not constant, Snell's law stops being accurate [4], so the generalized Snell's law should be used instead (see equation (1.1) with λ_0 being the wavelength of light in vacuum and $d\phi/dr$ is a spatial derivative of the phase-shift over the surface).

$$n_2 \sin(\theta_2) - n_1 \sin(\theta_1) = \frac{\lambda_0}{2\pi} \frac{d\phi}{dr} \tag{1.1}$$

A nanoparticle designed to change the phase of light is called a metaatom, and a metasurface is thereby a surface built using metaatoms in order to change the properties of light passing through it [1, 5]. One could note that the phase-shift and efficiency of the metaatom depends on its shape, size and rotation. This leads to the fact that two very different metaatoms in principle can achieve the same effects in the metasurface [1, 5, 6]. In order to create a light deflecting metasurface, one could manufacture a grating of metaatoms in order to bend light at an angle instead of using equation (1.1). This leads to the grating equation $n_2 \sin(\theta_2) - n_1 \sin(\theta_1) = o\lambda_0/P$, where P is the periodicity of the grating, and o is the diffraction order [1]. With the grating approach, the metaatoms sizes, positions and shapes only affect the amount of light that bends in any preferred direction, and not the deflection angle since $\Delta\phi/P = 2\pi/\lambda_0$.

1.1 Purpose and aim of thesis

As it takes some time and resources to manufacture nano-structures such as metasurfaces, it is wasteful to do optimizations through manufacturing each grating and experimentally confirming results. Therefore simulations are required in order to only manufacture structures that have potential to be good in the first place. As metasurfaces are usually made through stacking structures on top of a flat surface [1, 4, 7, 8], there are a few methods that can be used to simulate light propagation through these. Some simulation techniques are purely nummerical, such as FDTD (Finite Difference Time Domain), while others such as RCWA (Rigorous coupled wave analysis) are semianalytical [9].

Based on the deflection gratings, it has been shown that the S^4 program can use RCWA in order to optimize a structure that can be combined into a lens [1]. The semianalytical property of RCWA comes from the fact that it is a Fourier-based method [10]. Therefore the field propagation is calculated in frequency space, which works well if only one frequency is of interest [9]. It has also been shown that the RCWA method can calculate the same structures as the FDTD method [9, 10]. As multiple recent papers have been using FDTD simulations instead [7, 8, 11], the aim of this thesis is to evaluate and test whether the RCWA method through the S^4 program can hold up to other methods for optimization purposes.

2

Theory

As the Maxwell equations govern light propagation, the functionality of most (if not all) optical elements can be derived from these equations. Due to the fact that the S^4 program only handle non-magnetic materials, the permeability of the materials used will be assumed to be the vacuum permeability ($\mathbf{B} = \mu_0\mathbf{H}$). After deriving the wave equation from the Maxwell equations, some design approaches are stated. Finally the RCWA (Rigorous Coupled Wave Analysis) method used by the S^4 program is described.

2.1 The Maxwell equations

For optical components, it is important what happens to the electromagnetic fields inside of them. Therefore, the Maxwell equations are important to consider for any application. Note that for light in matter the Maxwell equations can be written like

$$\nabla \cdot \mathbf{D} = \rho_f \qquad \nabla \cdot \mathbf{B} = 0 \qquad \nabla \times \mathbf{E} = -\dot{\mathbf{B}} \qquad \nabla \times \mathbf{H} = \mathbf{J}_f + \dot{\mathbf{D}}$$

When working with optics, we are only interested in what happens to propagating light, and not on fields that the components create by themselves. We may therefore disregard the free charge ρ_f and free current charge $\mathbf{J}_f$ from the equations, meaning that we have

$$\nabla \cdot \mathbf{D} = 0 \qquad \nabla \cdot \mathbf{B} = 0 \qquad \nabla \times \mathbf{E} = -\dot{\mathbf{B}} \qquad \nabla \times \mathbf{H} = \dot{\mathbf{D}} \tag{2.1}$$

If we now assume that the materials are non-magnetic, we may note that $\mathbf{B} = \mu_0\mathbf{H}$ as μ_0 is the permeability in vacuum and that $\mathbf{D} = \epsilon\epsilon_0\mathbf{E}$ as ϵ_0 is the vacuum permittivity. So we find when assuming that ϵ is time-independent that

$$\nabla \times (\nabla \times \mathbf{E}) = -\mu_0 \frac{\partial}{\partial t} \nabla \times \mathbf{H} = -\mu_0 \ddot{\mathbf{D}} = -\mu_0\epsilon_0\epsilon\ddot{\mathbf{E}}$$

One may note that $\nabla \cdot \mathbf{E} = 0$ holds, since $\nabla \cdot \mathbf{D} = 0$. Therefore one may also note that $\nabla^2\mathbf{E} = \nabla(\nabla \cdot \mathbf{E}) - \nabla \times (\nabla \times \mathbf{E}) = -\nabla \times (\nabla \times \mathbf{E})$. Therefore we have (when

assuming that the permittivity tensor ϵ is time independent) that the **E**-field follows the wave equation:

$$\nabla^2 \mathbf{E} = \frac{\epsilon}{c_0^2} \ddot{\mathbf{E}} \tag{2.2}$$

as $\mu_0 \epsilon_0 = \frac{1}{c_0^2}$, and c_0 is the speed of light in vacuum.

2.2 Design approaches

When designing a metasurface, it should be designed such that the outgoing light has the required properties for the application. One way to do this is to create a phase map over the area that the metasurface will be [1, 12]. This can be constructed from the difference between the phase of the incoming field propagated to the metasurface, and the phase of desired field back-propagated to the metasurface. In turn this gives us the phase-shift $\varphi(x, y)$ that the metasurface should be designed for. Since this phase-shift becomes a map for construction of the metasurface, it may also be called a phase map.

2.2.1 Phase mapping approach

One popular way to create a metasurface is through the usage of the phase-mapping approach [5, 12, 13, 14, 15]. In this process, the phase-shift of a metaatom is calculated from simulation of that metaatom in an infinite sheet through periodic boundary conditions. Through iterating this process over a set of metaatoms, a set of building blocks for the metasurface is formed. By placing these building blocks on a grid based on which metaatom has a phase-shift that best matches the phase-map at the grid point, a metasurface is formed such that the phase-map of the metasurface approximates the required phase-map. As the metaatoms are small, the metasurface becomes approximately continuous at a larger scale.

Since the general way to measure light is through its intensity, a constant phase-shift over the surface will not lead to a measurable difference. Therefore only phase maps that change across the surface are considered. It has been shown that the phase mapping approach works well when the phase map changes slowly [1, 4, 16]. The approach works well since adjacent metaatoms would be similar to each other. When the phase map changes too fast, the efficiencies would generally decrease a lot [1, 11]. This effect could be explained by the fact that the periodic boundary conditions set for the building blocks do not hold. If the lattice would be commensurate with the periodicity of the phase map mod 2π, the metasurface could be explained using the grating approach instead.

2.2.2 Grating approach

As stated, the phase mapping approach becomes inefficient when the phase changes rapidly across the surface. This happens when there are not enough metaatoms to cover many places of the phase map when it shifts 2π, which in turn leads to a metasurface with an aperiodic patterning of metaatoms [1, 17]. The aperiodic

placements come from the fact that the metaatom lattice does not align with the distance required for 2π phase maps [1, 11]. In general, it is impossible to create a stationary lattice which would always align with the length of the 2π-shift, since the length of that segment will generally change over the entire metasurface.

Since the length of the 2π-shift of the phase-map will change across the surface, one might change the metaatom lattice in order to make it align with the metasurface. When one does that, it is noteworthy that one can identify a unit cell of metaatoms on the metasurface, where the periodicity is the same as the length of the 2π shift of the phase-map. If one may assume that the phase-map is approximately linear across the length of the unit cell, the created unit cell can be seen as a deflector as it deflects light in one direction.

One way to deflect light through transmission is through a regular grating. One may note that the grating equation for normal incidence ($d\sin(\theta) = m\lambda$) states the condition on the directions for maximum interference in a grating, given normal incidence. Note that this depends on the periodicity d, the deflection angle θ, the wavelength λ, and the deflection order m. One may however note that for a regular grating, the intensity of light going to the $m = +1$ order becomes equal to the intensity for light going in the $m = -1$ order. Using a regular grating as a deflector would therefore not be very beneficial, since it would get a low efficiency due to the fact that it spreads light in many directions. A metagrating could instead be designed in order to deflect most of the light in one direction and not in the other [1, 17]. Therefore the linear phase-shift of a deflector can be considered accurate for the metagrating.

One way to combat this aperiodic pattern is to change the periodicity of the lattice with the periodicity of the phase-shift [1]. This would then lead to increased efficiency of the metasurface when looking for the bending of light due to the grating equation. Therefore, the grating equation can be used since the part of the metasurface becomes a smarter grating.

2.2.3 Linear phase map

For a general phase map, there needs to be a way to know when one may assume that the phase map is linear. One way to do this is through looking at the wave equation we got from Maxwells equations earlier (2.2), and note that we may write the incoming **E**-field as $\mathbf{E}_i(\mathbf{x}, t) = \mathbf{E}_0 e^{i\phi(\mathbf{x},t)}$. This means that we need to solve the wave equation with a function that depends on $\exp(i\varphi(\mathbf{x}))$, which is reminiscent of the WKB approximation [18]. By using a similar approach to the WKB approximation, we may see that it is possible to make some predictions on when one may consider the phase map to be linear.

In general, light that goes through a metasurface would change phase, intensity and polarization [16]. This means that we may modulate the properties of transmitted light as

$$\mathbf{E}_t(x, y, z, t) = e^{i\varphi(x,y)} A_t(x, y)\mathbf{E}'(\mathbf{x}, t)$$

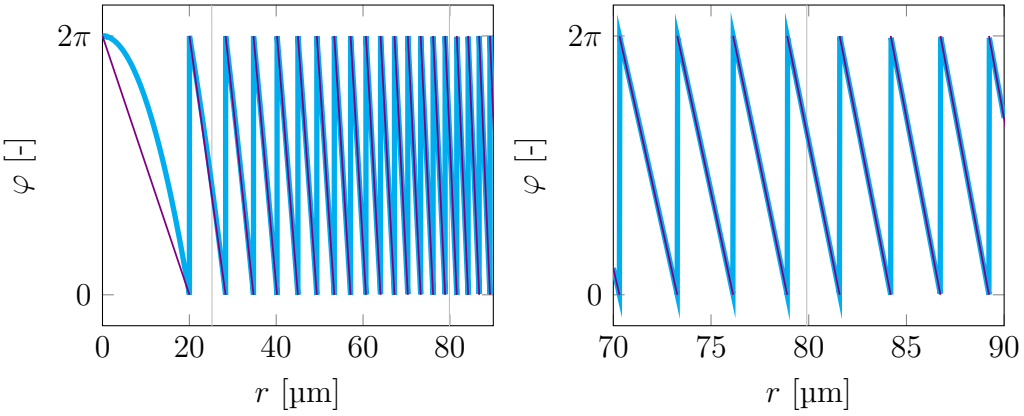

Figure 2.1: The phase-shift of a lens that bends light of a wavelength of 1 µm with a focal length of 200 µm is shown in cyan (mod 2π as $e^{i2\pi} = 1$). The phase shift of an ideal grating that bends light in one direction is shown in violet, where the size of the grating is chosen to be the distance between two consecutive points where the phase-shift is 2π. The points where the magnitude of the second derivative of the phase shift is equal to 10% and 1% respectively of the first derivative squared is marked with the gray vertical lines. Before the first gray line ($r \approx 25.2$ µm, corresponding to $\theta \approx 7.2°$), the phase-shift may not be considered linear on the scale of one grating. In between the two gray lines one may approximate the phase shift to be linear, but the periodicity changes noticeably from one grating to the next. After the second gray line ($r \approx 79.9$ µm, corresponding to $\theta \approx 21.8°$), the slope of the grating phase shift may even approximate the tangent slope of the lens phase shift at all points within the period.

where φ is the phase shift across the metasurface, A_t is the transmission coefficient of the $\mathbf{E}$-field, and $\mathbf{E}'(\mathbf{x}, t)$ is the transmitted field given no metasurface. Since the metasurface may change the polarization of light, A_t may become a tensor. Using the wave equation (2.2), we get $\nabla^2\mathbf{E} = \epsilon/c^2\ddot{\mathbf{E}}$, where ϵ is the permittivity tensor in the transmitted material. When assuming that A_t and φ are time independent since they come from material properties, the wave equation can be rewritten as

$$\nabla^2(e^{i\varphi(x,y)}A_t(x,y)\mathbf{E}'_i(\mathbf{x},t)) = \frac{\epsilon}{c^2}e^{i\varphi(x,y)}A_t(x,y)\ddot{\mathbf{E}}'_i(\mathbf{x},t)$$

We do however know that $\mathbf{E}'_i(\mathbf{x}, t)$ solves the wave equation as well, so we would find that

$$\nabla^2(e^{i\varphi(x,y)}A_t(x,y)\mathbf{E}'_i(\mathbf{x},t)) = e^{i\varphi(x,y)}\epsilon A_t(x,y)\epsilon^{-1}\nabla^2\mathbf{E}'_i(\mathbf{x},t)$$

Expanding the left hand side gives

$$(\nabla^2 e^{i\varphi})A_t\mathbf{E}'_i + 2(\nabla e^{i\varphi}\cdot\nabla)(A_t\mathbf{E}'_i) + e^{i\varphi}\nabla^2(A_t\mathbf{E}'_i) = e^{i\varphi}\epsilon A_t\epsilon^{-1}\nabla^2\mathbf{E}'_i$$

By noticing that $\nabla e^{i\varphi} = i(\nabla\varphi)e^{i\varphi}$ and that $\nabla^2 e^{i\varphi} = (i\nabla^2\varphi - (\nabla\varphi)^2)e^{i\varphi}$, we may now rewrite the equation into

$$(i\nabla^2\varphi - (\nabla\varphi)^2)A_t\mathbf{E}_i' + 2(\nabla\varphi\cdot\nabla)(A_t\mathbf{E}_i') + \nabla^2(A_t\mathbf{E}_i') = \epsilon A_t\epsilon^{-1}\nabla^2\mathbf{E}_i'$$

If the phase shift is linear, one finds that $\nabla^2\varphi = 0$. When looking at the first term, the linear approximation would mean that $(i\nabla^2\varphi - (\nabla\varphi)^2)A_t\mathbf{E}_i' \approx -(\nabla\varphi)^2 A_t\mathbf{E}_i'$. In order to justify this approximation, we need to state that $|\nabla^2\varphi| \ll |\nabla\varphi|^2$.

For the example that a lens was designed, then the required phase map for the metasurface becomes $\varphi(r) = -\frac{2\pi}{\lambda}(\sqrt{r^2+f^2} - f)$. This means that we would get $\nabla\varphi = -\frac{2\pi}{\lambda}\frac{r}{\sqrt{r^2+f^2}}\hat{r}$ and $\nabla^2\varphi = -\frac{2\pi}{\lambda}\frac{r^2+2f^2}{\sqrt{r^2+f^2}^3}$. In the end this tell us that we require $\frac{\lambda(r^2+2f^2)}{2\pi r^2\sqrt{r^2+f^2}} \ll 1$, or if we want to look at the radius as a function of the deflection angle θ, we have $r = f\tan(\theta)$, which means that we may rewrite the requirement as $\cos(\theta) + 2\frac{\cos^3(\theta)}{\sin^2(\theta)} \ll \frac{2\pi f}{\lambda}$. Using a wavelength of $\lambda = 1$ µm and focal length of $f = 200$ µm, the phase map can be seen in figure 2.1. The phase map could be considered linear at deflection angles of $\theta > \theta_{\min} \approx 21.8°$ or larger given that the second order differentiation should give a contribution to the wave equation less than 1% of what the first order gives. (For a contribution of less than 10%, we would get $\theta > \theta_{\min} \approx 7.2°$.)

2.3 RCWA

This section will handle the theory behind the S^4 program, which simulates light propagation through non-magnetic structures with the RCWA (Rigorous Coupled Wave Analysis) method. This means that this chapter is heavily inspired by the paper that introduced S^4. [10]

RCWA or FMM (Fourier Modal Method) is a semianalytical way to calculate fields for layered structures in a lattice. The method starts by looking at the Maxwell equations for light propagation in matter (see equations (2.1)), and assuming that the EM fields are PMWs (Plane Monochromatic Waves) inside non-magnetic materials. This means that the time derivative may be replaced by $-i\omega$, and that $\mu = 1$, giving the simpler equations seen below.

$$\nabla\times\mathbf{H} = -i\omega\epsilon_0\epsilon\mathbf{E} \qquad\qquad \nabla\times\mathbf{E} = i\omega\mu_0\mathbf{H}$$

Since the layered structure is in a lattice, we may use the periodicity in order to write the structure as a 2D Fourier series in the plane normal to the direction that the stacking of the layers occur (the xy-plane). This means that as $\mathbf{r} = [x, y]^T$, we may write the fields as

$$\mathbf{E}(\mathbf{r}, z) = \sum_{\mathbf{G}} \mathbf{E}_{\mathbf{G}}(z)e^{i\mathbf{k}\cdot\mathbf{r}}e^{i\mathbf{G}\cdot\mathbf{r}} = \sum_{\mathbf{G}} \mathbf{E}_{\mathbf{G}}(z)e^{i(\mathbf{k}+\mathbf{G})\cdot\mathbf{r}} \tag{2.3}$$

where $\mathbf{k} = [k_x, k_y]$ is the wave-vector projected on the xy-plane, and $\mathbf{G}$ is a 2D reciprocal lattice vector. Note that we get the same form on the $\mathbf{B}, \mathbf{D}$ and $\mathbf{H}$-fields as for the $\mathbf{E}$-field. This gives an infinite sum, which unfortunately is difficult to calculate. For most systems however, there exists a point where adding more $\mathbf{G}$-vectors does not give any meaningful change in the fields. Therefore, the infinite sum can be approximated by a finite sum where the terms used is inside of a circle in reciprocal space with radius r_k ($|\mathbf{G}_n| < r_k, \forall n < N_G$, where N_G is the number of $\mathbf{G}$-vectors). Therefore, a larger number of $\mathbf{G}$-vectors gives a better approximation of the fields.

The two dimensional Fourier-transform of a component X becomes

$$\hat{X}(\mathbf{G}) = \frac{1}{A_l} \iint_{\text{lattice}} X(\mathbf{r}) e^{-i\mathbf{G}\cdot\mathbf{r}} d\mathbf{r}$$

where A_l is the area of the lattice. By Fourier-transforming the fields, we see that $\hat{\mathbf{E}}(\mathbf{G}', z) = \mathbf{E}_{\mathbf{G}}(z)\delta(\mathbf{G} + \mathbf{k} - \mathbf{G}')$. Let us now discretize $\mathbf{G}'$ such that $\mathbf{G}$ and $\mathbf{G}'$ come from the same set of G-vectors in order to later be able to compute the Maxwell equations. This means that

$$\hat{\mathbf{E}}_{\mathbf{G}'}(z) = \mathbf{E}_{\mathbf{G}}(z)\delta_{\mathbf{G}+\mathbf{k},\mathbf{G}'}$$

Note that $\mathbf{D} = \epsilon_0 \epsilon \mathbf{E}$, which means that we can Fourier-transform both sides, where we see that the LHS becomes $\hat{\mathbf{D}}_{\mathbf{G}'}(z) = \mathbf{D}_{\mathbf{G}}(z)\delta_{\mathbf{G}+\mathbf{k},\mathbf{G}'} = \mathbf{D}_{\mathbf{G}'-\mathbf{k}}(z)$, and the RHS becomes $\sum_{\mathbf{G}} \epsilon_0 \hat{\epsilon}_{\mathbf{G}+\mathbf{k}-\mathbf{G}'} \mathbf{E}_{\mathbf{G}}$. We may therefore write

$$\mathbf{D}_{\mathbf{G}-\mathbf{k}} = \sum_{\mathbf{G}'} \epsilon_0 \hat{\epsilon}_{\mathbf{G}'+\mathbf{k}-\mathbf{G}} \mathbf{E}_{\mathbf{G}'} = \sum_{\mathbf{G}'} \epsilon_0 \hat{\epsilon}_{\mathbf{G}',\mathbf{G}-\mathbf{k}} \mathbf{E}_{\mathbf{G}'} \Rightarrow \mathbf{D}_{\mathbf{G}} = \sum_{\mathbf{G}'} \epsilon_0 \epsilon_{\mathbf{G}',\mathbf{G}} \mathbf{E}_{\mathbf{G}'}$$

when we set $\hat{\epsilon}_{\mathbf{G},\mathbf{G}'} = \hat{\epsilon}_{\mathbf{G}-\mathbf{G}'}$. Since we require that the z-components can be separated from the fields, the most general permittivity tensor that this method can use looks like

$$\epsilon = \begin{bmatrix} \epsilon_{xx} & \epsilon_{yx} & 0 \\ \epsilon_{xy} & \epsilon_{yy} & 0 \\ 0 & 0 & \epsilon_z \end{bmatrix}$$

This lets us note that $D_z = \epsilon_0 \epsilon_z E_z$ or equivalently $D_{\mathbf{G},z} = \sum_{\mathbf{G}'} \epsilon_0 \hat{\epsilon}_{z,\mathbf{G}',\mathbf{G}} E_{\mathbf{G}',z}$, where $\hat{\epsilon}_{z,\mathbf{G}',\mathbf{G}}$ is the Fourier-transform of ϵ_z. We may now write out the complete Maxwell equations.

$$\begin{aligned}
\frac{\partial H_z}{\partial y} - \frac{\partial H_y}{\partial z} &= -i\omega D_x \\
\frac{\partial E_z}{\partial y} - \frac{\partial E_y}{\partial z} &= i\omega\mu_0 H_x \\
\frac{\partial H_x}{\partial z} - \frac{\partial H_z}{\partial x} &= -i\omega D_y \\
\frac{\partial E_x}{\partial z} - \frac{\partial E_z}{\partial x} &= i\omega\mu_0 H_y \\
\frac{\partial H_y}{\partial x} - \frac{\partial H_x}{\partial y} &= -i\omega\epsilon_0\epsilon_z E_z \\
\frac{\partial E_y}{\partial x} - \frac{\partial E_x}{\partial y} &= i\omega\mu_0 H_z
\end{aligned}$$

If we now use the series expansion of the fields (see equation (2.3)) and Fourier-transform the equations, we may find that $\frac{\partial}{\partial x}$ and $\frac{\partial}{\partial y}$ becomes $i\hat{k}_{x,\mathbf{G}}$ and $i\hat{k}_{y,\mathbf{G}}$ respectively after the Fourier-transform, where $\hat{k}_{x,\mathbf{G}} = (k_x + G_x)$ (and similarily for $\hat{k}_{y,\mathbf{G}}$). Since we do not Fourier-transform in the z-direction, $\frac{\partial}{\partial z}$ becomes iq since we have assumed that the field is a PMW ($\mathbf{E}_\mathbf{G}(z) \propto e^{iqz}$) as q is the z-component of the wave vector. The Fourier-transformed Maxwell equations therefore look like

$$\begin{aligned}
\hat{k}_{y,\mathbf{G}} H_{z,\mathbf{G}} - qH_{y,\mathbf{G}} &= -\omega D_{x,\mathbf{G}} \\
\hat{k}_{y,\mathbf{G}} E_{z,\mathbf{G}} - qE_{y,\mathbf{G}} &= \omega\mu_0 H_{x,\mathbf{G}} \\
qH_{x,\mathbf{G}} - \hat{k}_{x,\mathbf{G}} H_{z,\mathbf{G}} &= -\omega D_{y,\mathbf{G}} \\
qE_{x,\mathbf{G}} - \hat{k}_{x,\mathbf{G}} E_{z,\mathbf{G}} &= \omega\mu_0 H_{y,\mathbf{G}} \\
\hat{k}_{x,\mathbf{G}} H_{y,\mathbf{G}} - \hat{k}_{y,\mathbf{G}} H_{x,\mathbf{G}} &= -\omega\epsilon_0 \sum_{\mathbf{G}'} \hat{\epsilon}_{z,\mathbf{G}',\mathbf{G}} E_{z,\mathbf{G}'} \\
\hat{k}_{x,\mathbf{G}} E_{y,\mathbf{G}} - \hat{k}_{y,\mathbf{G}} E_{x,\mathbf{G}} &= \omega\mu_0 H_{z,\mathbf{G}}
\end{aligned}$$

If we look at these equations as matrix and vector equations in $\mathbf{G}$-space, we see that $\hat{k}_{x,\mathbf{G}}$ and $\hat{k}_{y,\mathbf{G}}$ need to be diagonal matrices. We also see that $\hat{\epsilon}_{z,\mathbf{G}',\mathbf{G}}$ can be written as a matrix, as well as $H_{i,\mathbf{G}}$, $E_{i,\mathbf{G}}$ and $D_{i,\mathbf{G}}$ can be vectors. If we do this, we may disregard $\mathbf{G}$ in the notation. Using lower-case letters in order to not mix up the vectors in $\mathbf{G}$-space and the real fields. Using this, we find

$$\hat{k}_y h_z - qh_y = -\omega d_x \tag{2.4}$$
$$\hat{k}_y e_z - qe_y = \omega\mu_0 h_x \tag{2.5}$$
$$qh_x - \hat{k}_x h_z = -\omega d_y \tag{2.6}$$
$$qe_x - \hat{k}_x e_z = \omega\mu_0 h_y \tag{2.7}$$
$$\hat{k}_x h_y - \hat{k}_y h_x = -\omega\epsilon_0 \hat{\epsilon}_z e_z \tag{2.8}$$
$$\hat{k}_x e_y - \hat{k}_y e_x = \omega\mu_0 h_z \tag{2.9}$$

Using equation (2.8), we may cancel e_z from equations (2.5) and (2.7), which gives us

$$\omega^2\mu_0 h_x - \frac{\hat{k}_y\hat{\epsilon}_z^{-1}}{\epsilon_0}\left(\hat{k}_y h_x - \hat{k}_x h_y\right) = -\omega q e_y$$
$$\omega^2\mu_0 h_y - \frac{\hat{k}_x\hat{\epsilon}_z^{-1}}{\epsilon_0}\left(\hat{k}_x h_y - \hat{k}_y h_x\right) = \omega q e_x$$

These two equations can be combined into one matrix-vector expression, seen in equation (2.10).

$$(\omega^2\mu_0 I - \kappa)\begin{bmatrix} h_x \\ h_y \end{bmatrix} = \omega q \begin{bmatrix} -e_y \\ e_x \end{bmatrix} \tag{2.10}$$

where κ is defined as

$$\kappa = \frac{1}{\epsilon_0}\begin{bmatrix} \hat{k}_y\hat{\epsilon}_z^{-1}\hat{k}_y & -\hat{k}_y\hat{\epsilon}_z^{-1}\hat{k}_x \\ -\hat{k}_x\hat{\epsilon}_z^{-1}\hat{k}_y & \hat{k}_x\hat{\epsilon}_z^{-1}\hat{k}_x \end{bmatrix}$$

Using equation (2.9) in a similar manner in order to cancel h_z from equations (2.4) and (2.6) gives

$$-\omega^2 d_y - \frac{\hat{k}_x}{\mu_0}\left(\hat{k}_x(-e_y) + \hat{k}_y e_x\right) = \omega q h_x$$
$$\omega^2 d_x - \frac{\hat{k}_y}{\mu_0}\left(\hat{k}_x(-e_y) + \hat{k}_y e_x\right) = \omega q h_y$$

which, rewritten in matrix form looks like

$$\omega^2\begin{bmatrix} -d_y \\ d_x \end{bmatrix} - K\begin{bmatrix} -e_y \\ e_x \end{bmatrix} = \omega q \begin{bmatrix} h_x \\ h_y \end{bmatrix} \tag{2.11}$$

with

$$K = \frac{1}{\mu_0}\begin{bmatrix} \hat{k}_x\hat{k}_x & \hat{k}_x\hat{k}_y \\ \hat{k}_y\hat{k}_x & \hat{k}_y\hat{k}_y \end{bmatrix}$$

Recalling that in the spatial coordinates, the permittivity equation looks like $\mathbf{D} = \epsilon\mathbf{E}$. Since we can separate the z-directional field, we may define a $2N_G \times 2N_G$ matrix ε as

$$\varepsilon = \begin{bmatrix} \hat{\epsilon}_{yy,\mathbf{G}',\mathbf{G}} & \hat{\epsilon}_{xy,\mathbf{G}',\mathbf{G}} \\ \hat{\epsilon}_{yx,\mathbf{G}',\mathbf{G}} & \hat{\epsilon}_{xx,\mathbf{G}',\mathbf{G}} \end{bmatrix}$$

By doing that, the Fourier-transformed counterpart of the permittivity equation would look like

$$\begin{bmatrix} -d_y \\ d_x \end{bmatrix} = \varepsilon \begin{bmatrix} -e_y \\ e_x \end{bmatrix}$$

Using the Fourier-transformed permittivity equation, we can simplify equation (2.11) to

$$(\omega^2\varepsilon - K)\begin{bmatrix}-e_y\\ e_x\end{bmatrix} = \omega q\begin{bmatrix}h_x\\ h_y\end{bmatrix} \tag{2.12}$$

If we now assume that $\mathbf{H}$ is on the form

$$\mathbf{H}_{\mathbf{G}}(z) = (\phi_{x,\mathbf{G}}\hat{x} + \phi_{y,\mathbf{G}}\hat{y} + \phi_{z,\mathbf{G}}\hat{z})e^{iqz}$$

we may note that we may use the Fourier-transformed Maxwell equations in order to solve for $\phi_{z,\mathbf{G}}$, which means that we find

$$\phi_{z,\mathbf{G}} = -\frac{k_x + G_x}{q}\phi_{x,\mathbf{G}} - \frac{k_y + G_y}{q}\phi_{y,\mathbf{G}}$$

from the equations that come from the rotation of the $\mathbf{E}$-field. If we again use the vector approach (let us state that ϕ_x is a vector in $\mathbf{G}$-space that contains $\phi_{x,\mathbf{G}}$), we note that

$$\mathbf{h} = \left[\phi_x\hat{x} + \phi_y\hat{y} - \left(\frac{\hat{k}_x\phi_x}{q} + \frac{\hat{k}_y\phi_y}{q}\right)\hat{z}\right]e^{iqz}$$

Using this together with equations (2.10) and (2.12), we find that

$$\begin{aligned}(\omega^2\mu_0 I - \kappa)\begin{bmatrix}\phi_x\\ \phi_y\end{bmatrix}e^{iqz} &= \omega q\begin{bmatrix}-e_y\\ e_x\end{bmatrix}\\ (\omega^2\varepsilon - K)\begin{bmatrix}-e_y\\ e_x\end{bmatrix} &= \omega q\begin{bmatrix}\phi_x\\ \phi_y\end{bmatrix}e^{iqz}\end{aligned}$$

By combining the equations and defining $\boldsymbol{\phi}$ as $\boldsymbol{\phi} = [\phi_x, \phi_y]^T$ we may find that this becomes

$$\frac{1}{\omega^2}(\omega^2\mu_0 I - \kappa)(\omega^2\varepsilon - K)\boldsymbol{\phi} = (\varepsilon(\omega^2 - \kappa) - K)\boldsymbol{\phi} = q^2\boldsymbol{\phi} \tag{2.13}$$

since $\kappa K = 0$. So we have reduced solving the Maxwell equations into eigenvalue calculations of a $2N_G \times 2N_G$ matrix, where N_G is the number of $\mathbf{G}$-vectors to sum over. Solving this equation is the most time-consuming part, and scales with the number of $\mathbf{G}$-vectors as N_G^3. This is then done for each layer, giving a total solving time that scales as MN_G^3, where M is the number of layers in the structure.

We may now define the forward propagation amplitude a_n and backward propagation amplitude b_n inside layer i and for $\mathbf{G} = \mathbf{G}_n$ through

$$\begin{bmatrix}h_x(z)\\ h_y(z)\end{bmatrix} = \sum_n \begin{bmatrix}\phi_{x,n}\\ \phi_{y,n}\end{bmatrix}(a_n e^{iq_n(z-z_i)} + b_n e^{iq_n(d_i-(z-z_i))})$$

with $\phi_{x,n} = \phi_{x,\mathbf{G}_n}$ while z_i and d_i is the height and thickness of layer i respectively. Then the fields can be recrea able to recreate the fields through

$$\begin{bmatrix} e_{t,n}(z) \\ h_{t,n}(z) \end{bmatrix} = \begin{bmatrix} (\omega^2 I - \kappa)\boldsymbol{\phi}_n q_n^{-1} & -(\omega^2 I - \kappa)\boldsymbol{\phi}_n q_n^{-1} \\ \boldsymbol{\phi}_n & \boldsymbol{\phi}_n \end{bmatrix} \begin{bmatrix} e^{iq_n(z-z_i)} a_n \\ e^{iq_n(d_i-(z-z_i))} b_n \end{bmatrix}$$

Note that each eigenvector $\boldsymbol{\phi}_n = [\phi_{x,n}, \phi_{y,n}]^T$ has a corresponding eigenvalue q_n^2 together with propagation amplitudes a_n and b_n. As a_n and b_n decides the propagation direction, only the solution where $q_n = \sqrt{q_n^2}$ is used in the equation above. The fields can be found from the left hand side through $e_{t,n}(z) = [-e_{y,n}(z), e_{x,n}(z)]^T$ and $h_{t,n}(z) = [h_{x,n}(z), h_{y,n}(z)]^T$. This can then be solved for all $n \in [1, 2, \dots N_G]$, which later can be used to find the fields in the end. From this, the **H**-field propagating along the direction $\hat{k}'$ can be recreated through equation (2.14), while the **E**-field can be found as $\mathbf{E} = \mathbf{H} \times \hat{k}'/n$ [19].

$$\mathbf{H} = \sum_{n=1}^{N_G} \left(h_{x,n}(z) \left(\hat{x} - \hat{z}\frac{\hat{k}' \cdot \hat{x}}{\hat{k}' \cdot \hat{z}} \right) + h_{y,n}(z) \left(\hat{y} - \hat{z}\frac{\hat{k}' \cdot \hat{y}}{\hat{k}' \cdot \hat{z}} \right) \right) e^{i((\mathbf{k}+\mathbf{G_n})\cdot\mathbf{r})-\omega t} \tag{2.14}$$

3

Method

In this chapter, the methods used will be presented. The first section describes how the simulations were made, except for specific details stated in the next chapter (chapter 4). Since the simulation method was changed slightly for the different results, it is described in the order of lens recreation, S^4 validation and ending with the optimized deflectors. After the simulation section comes a section about the optimization algorithm. Then a section about how the gratings and center piece was put together into a lens. The chapter ends with the setup for the experimental measurements done on the optimized deflectors.

3.1 Simulation

All simulations in this project were done by a S^4 program, using the RCWA method described in section 2.3. A Lua script was used in order to communicate between a Python script and the S^4 program. Given a structure to simulate, the Python script generated two text files, one containing a list of elliptical metaatoms and another file containing lattice information, indices of refraction and metaatom height among other data needed to do the simulation. The list of elliptical metaatoms contained a row for each metaatom and five columns of properties (see section A). This list will in this thesis be called a xyrra-list due to the properties listed being position (x,y), halfwidths (r_x,r_y) and rotation angle (a) of the metaatoms. These files where then read by the Lua script, which could talk directly with the S^4 program, in which the simulations were done. The output of the Lua script could then be passed down to the Python script again as an output and exception parameter, which was translated into data that could be analyzed.

Depending on the task at hand, different Lua scripts were used. For the lens recreations (section 4.1), the instructions given to the S^4 program from the Lua script were to have a plane wave in air to be incoming with an incident angle. The efficiency given a polarisation was found through calculating the intensities from the imaginary part of the magnetic field as $\mathbf{H} = H_x(\hat{x} - \hat{z}k_x/k_z) + H_y(\hat{y} - \hat{z}k_y/k_z)$ [19]. Depending on the polarization studied, the Poynting vector ($\mathbf{S} = \mathbf{E} \times \mathbf{H}^*/2$) will either depend on $|H_x|^2$ or $|H_y|^2$. Since the phase is the argument of the fields, the normalization will remove the phase dependence. In order to make sure the gratings do not interfere with each other when combined into the lens, the optimization used

$H_{x,\mathrm{Im}}|H_{x,\mathrm{Im}}|$ instead of $|H_x|^2$, and similarly with H_y. This made sure that the fields interfered constructively in the focal point[1]. In order to get the total efficiency, the average of the efficiencies for the different polarizations were used.

In order to collect the wavelength spectra (figure 4.8) for the grating seen in figure 4.7, the instructions given to the S^4 program had to change. Therefore, a new Lua script was created where the incoming light going along the optical axis (normal incidence) was deflected instead of deflecting light onto the optical axis. Another change was that the Lua script outputted efficiencies for both polarizations at the same time instead of requiring to do the same simulation once for each polarization. Then the biggest change was that the forward amplitude was not sufficient in order to create these figures, since the efficiencies became nonphysical when the wavelength became larger than the periodicity of the grating. Instead the power flux was extracted from the S^4 program per order of diffraction. Efficiency calculations were done through dividing the power diffracted through a specific order with the incident power. The phase of the outgoing field was discarded due to the grating already being optimized.

For optimizing the gratings in section 4.3, the same Lua script was used as the one used in section 4.2, but only the p polarized (**H**-field perpendicular to the deflection direction of the grating) light deflected to the +1 order was returned instead of all orders and polarizations. Since the surface was filled with the same grating, the outgoing light in each deflection order becomes collimated. If multiple gratings were to be used, and the phase of the light needed to be equal at some distance away from the grating, the phase could be extracted from the forward scattered amplitude when using the power flux for the intensity part of the efficiency.

3.2 Optimization

The optimization process could be characterized for each grating by a random walk along a multidimensional gradient, where each elliptical cylinder in the grating contribute to five dimensions in this space. Two dimensions for the center position, two dimensions for the different radii of the ellipse and one dimension for the angle it is rotated around its center. One may now note that there are an infinite number of equivalent positions due to rotational periodicity of 360 degrees, position periodicity in the x- and y-direction, and if all cylinders are translated by the same vector. These equivalences are not taken into account however, since one optimal solution is enough.

Two optimization processes have been used in order to find the optimal solution. One rough optimization that first chooses a dimension to go along randomly (of the dimensions not yet tried), and then if that dimension happens to be an angle, the value will change with $\pm 3°$, otherwise it changes with ± 10 nm. Then the new grating is simulated, the efficiency is compared with the current grating, and the lower efficiency grating is discarded. The grating was considered optimized when no singular change would give a better efficiency. When that has been done, the same

process is started again, but this time for a finer value change of $\pm.3°$ and ±1 nm.

When the grating was optimized with the first optimization process, another random optimization takes place in order to fine tune the optimization. Now, the optimization goes a random distance smaller than .3° or 1 nm in each dimension at the same time, and then compares the efficiencies to discard the less efficient one. This time, the grating is considered optimized after a given number of attempts has been made. For the first grating in each collection, 400 attempts were used, and the rest were optimized with 200 attempts instead.

3.3 From optimized deflection gratings to a lens

Due to the simulation calculating the efficiency of the grating from an infinite array, gratings adjacent to each other need to be similar in order to have the simulated efficiency be somewhat close to the actual efficiency. In order to create a lens from deflectors, the deflection angles need to vary over the radius of the lens. Therefore, a collection of gratings was created with one optimized grating as a starting point. For each new grating, the xyrra list was copied over from the latest grating in the collection to a new grating with different lattice coefficients.

The new lattice coefficients corresponded to a 1% increase in width, and a decrease in length change corresponding such that $W \propto \tan(\sin^{-1}(\lambda/L))$ [1] where W and L is the width and length of the grating respectively. With the new lattice, the new grating was then optimized with the constraint that the xyrra list does not change more than 3% of the initial list. The optimization methods used were only the fine version of the first method together with 200 attempts of the second method in order to save computation time. When the deflection angle of the next grating would be larger than the designated end angle, the collection of gratings was considered complete.

As the length of the gratings get smaller for larger deflection angles, less metaatoms fit inside of the lattice. Therefore, it is not reasonable that the entire lens can be built on one center piece, and one grating collection. Instead, four different grating collections were optimized with different starting width, number of metaatoms per grating, start and end angles. The first collection contained gratings with five metaatoms per grating and deflection angles from 20° to 31°, and the first grating had a width of 350 nm. Using the same width on the first grating, the second collection contained gratings with four metaatoms and deflection angles between 31° and 45°. With a starting width of 300 nm, the third collection contained gratings with two metaatoms per grating and deflection angles between 45° and 55°. The fourth grating also contained two metaatoms, but deflection angles between 65° and 70°. Notice that as there was a gap in deflection angles between the third and the fourth collection, the fourth was not used to create a lens.

When the grating collections were optimized, the center of the lens was created using 20 circular cylindrical metaatoms with evenly spaced radii between 100 and 200 nm

and a height equal to the cylinder height used for the grating collections (550 nm). Then a hexagonal grid was created where the shortest distance between grid points were 300 nm. The phase shift from each of these metaatoms were calculated from simulations. At each grid point on the hexagonal grid the phase map was calculated and compared to each of the 20 metaatoms, where the metaatom with the most similar phaseshift was chosen to be placed at that point.

Combining the center with the grating collections was done through placing the grating collections in rings around the hexagonal patterning. Each collection consisted of thinner rings of metaatoms, where the deflection grating that has the best matching deflection angle to the placement of the ring was copied around the circumference of that circle. This was repeated until the radius of the lens got larger than 285 µm. With a focal length of 200 µm, this means that the maximum deflection angle used in the lens would become approximately 54.9°.

3.4 Experimental setup for measurements

The experimental setup for measuring the angles and the efficiency of the gratings was built by Einstom Engay and consisted of a white light lamp combined with a 1064 nm linearly polarized laser. The light was then collimated and sent through a beam shutter in order to make sure that the beam could be approximated to a plane wave while only exciting the intended metasurface, since multiple surfaces was etched on one substrate. The light then encountered the glass substrate with the metasurfaces on it, which could be translated in three directions, x and y direction for choice of metasurface, and z direction for focusing. After the light went through the desired point on the glass surface, it continued through a magnification objective and then through an objective lens which focuses the light onto the camera such that the magnification became 61 times the starting image. A beam-splitter was placed in between the lens and the first camera, such that the light could be sampled from the first camera could be sampled from another simultaneously. See figure 3.1.

As two cameras were used, multiple things could be measured at the same time. One camera was used to capture the image plane such that it was possible to see the part of the surface hit by the laser and if the surface was placed in the focal plane or not. This made it possible to translate the surface in order to choose which metasurface to measure. The other camera took pictures in the Fourier-plane where the pixel position depends on the incoming angle of light to the camera. This means that the distance Δx can be related to the incoming angle γ as $\Delta x = f \tan(\gamma)$, where f is the focal length of the Fourier-lens. In the setup, we have a objective with a very short working distance and a lens with a comparatively large focal length, which leads to angles that are reduced by a large factor. Since the angles are reduced by a factor R, we may note that $\gamma = \theta/R$ for a deflection angle of θ. Since R is large, one may note that $\tan(\theta/R) \approx \theta/R$, giving the realization that $\Delta x \propto \theta$.

Using this with the pixel value for the zero order peak, one could measure the angles from the picture of the Fourier image given the proportionality constant between

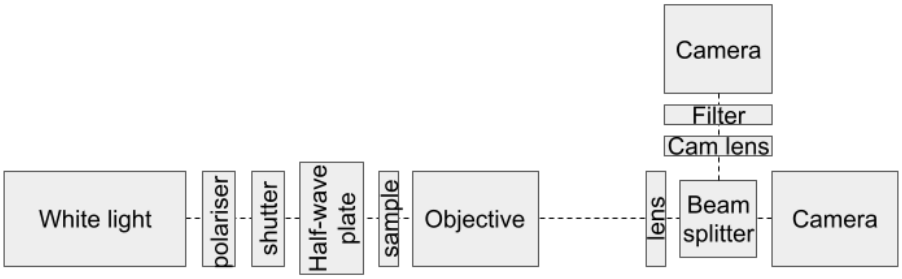

Figure 3.1: A sketch of how the setup looked like. First, linearly polarized white light went through a shutter, in order to get more collimated light to the sample, as well as not hitting other samples as well as the intended sample. A half-wave plate was used in order to make sure the polarization was oriented in line with the sample. When the light passed through the half-wave plate, it went through the metasurface sample, through oil and into the oil immersion objective. The light then traveled through a lens, and into a CCD camera such that the image plane is in the camera plane. A beamsplitter was then placed in between the lens and the camera, such that a camera lens with a focal length of 50 mm was placed such that the Fourier plane could be picked up by the other CCD camera after a band pass filter that only let light close to 1064 through.

Δx and θ, and the intensities through summation of the pixel values around the maximum value, until the value got smaller than the maximum/e^2. The Fourier image camera could be controlled by an exposure time, which stated the time that photons could reach the camera before picture is refreshed. The different figures made with the Fourier image camera used different exposure times, since the peak is difficult to see when the exposure time is too low, and if the exposure time is too high, the camera pixel get saturated. However, due to the photon rate being approximately constant, the number of photons seen is linear with the exposure time, so the efficiency was then calculated as the number of photons per exposure time in the +1 order divided by the transmitted number of photons per exposure time when there was no metasurface on the SiO_2 substrate.

4

Results

In this chapter, various results found during the project will be shown. Firstly, a recreation of a part of the lens from J. Byrnes et al. [1] was attempted. Since that was driven by random optimizations, it was difficult to use that data in order to characterize the S^4 program as a whole. Therefore, one grating that Paniagua-Domínguez et al. [2] had optimized was simulated by the S^4 program, and similar results were found to those they had. Finally some new gratings were optimized and tested in order to compare how well the program aligns to real experiments.

4.1 Recreating a lens

J. Byrnes [20] used some Python scripts, together with a precompiled version of the S^4 program [10] in order to simulate a large NA lens made of 550 nm tall TiO_2 metaatoms on a SiO_2 substrate [1]. With the help of these scripts, an attempt to recreate a few grating collections from their paper was done. The efficiency distribution can be seen in figure 4.1, and was not as impressive as their results, but close enough that some random deviations or other misinterpretations could be the cause for the inconsistencies.

Since the S^4 program uses the RCWA method, the permittivity of the metaatoms will not have very sharp transitions on the edges of the metaatoms, due to dismissing the higher order Fourier terms. Therefore, the permittivity was traced in order to estimate how accurate one can assume the S^4 program to be. The precompiled version of the S^4 program used by Byrnes et al. [1] gave error messages when trying to create the permittivity map, so in order to create this figure (figure 4.2), the latest version of the S^4 program was downloaded from the S^4 git repository [10, 21] and compiled into a .exe file through Cygwin64. This reconfiguration led to a significant upgrade in computation speed, and some different results in efficiency (compare figure 4.4 with figure 4.3). Another bug in the old version that got solved in the new version was that the old version would crash when using too many G-vectors.

As stated previously, the efficiency of the gratings changed drastically when using the new program compared to the old (compare figure 4.3 with figure 4.1). This is especially true when using the same number of G-vectors. However, since the permittivity map (figure 4.2) get closer to the value given to the S^4 program when

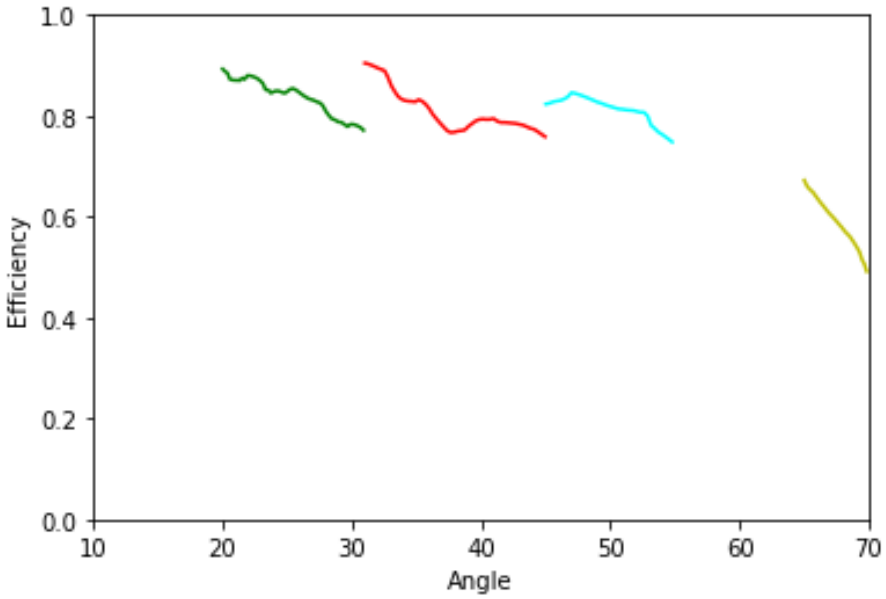

Figure 4.1: The efficiency spectrum of the lens, using the old version of the S^4 program, and 100 G-vectors. What is seen here is the average of the efficiencies of s- and p-polarizations when deflecting light incoming at an incident angle to the optical axis. Every color represents a different grating collection, generated from the grating with the lowest angle grating, such that the adjacent gratings are similar to each other. Because I could not figure out how the gratings looked between 55° and 65° in the paper from Byrnes et al.[1], I did not make a grating collection between these angles. Note that this distribution of gratings are qualitatively similar to the same parts of figure 4a in [1].

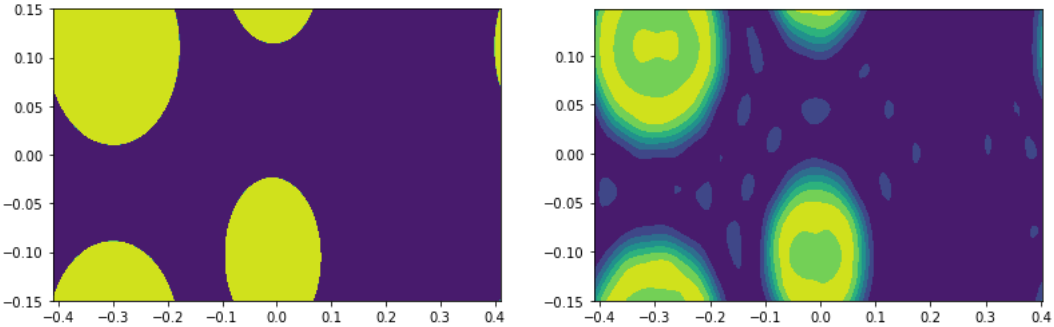

Figure 4.2: The permittivity map for one grating, the left figure is the permittivity map fed to the S^4 program at wavelength $\lambda = 580$ nm for elliptical cylinders of TiO_2 in air. The right figure is the permittivity map after the Fourier series approximation when using 200 G-vectors. Yellow means that the permittivity is $\epsilon \approx 5.626$, and deep blue means that the permittivity is $\epsilon \approx 1$. When increasing the number of G-vectors, the edges between different permittivities in the right image become more sharp.

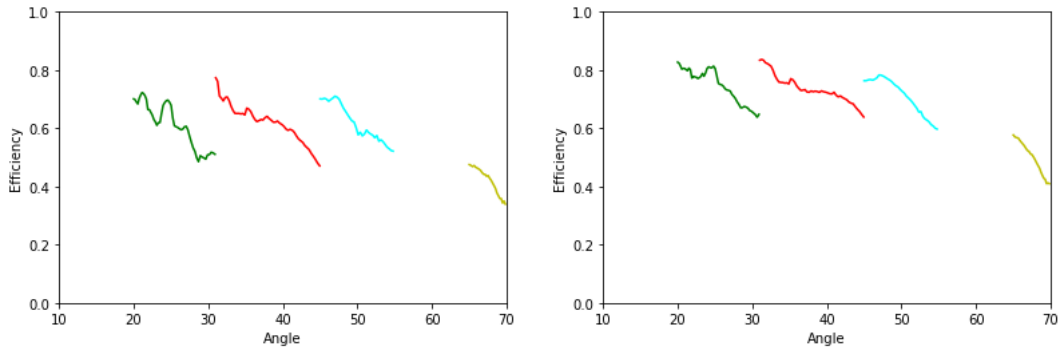

Figure 4.3: The same grating collections as in 4.1, but this time the updated version of the S^4 program was used to calculate the efficiencies. In the left figure, the number of G-vectors was the same (100), and in the right figure more G-vectors was included (a total of 300 G-vectors) in order to get a better approximation of the actual efficiencies when using the new S^4 program

increasing the number of G-vectors, one should only consider the results when the efficiency has converged for the number of G-vectors [10]. Since the efficiencies shown for 300 G-vectors was very similar to the efficiencies when 400 G-vectors was used, these results may be considered converged.

After the analysis of the gratings created with the old program, some new grating collections were optimized with the same conditions by using the new S^4 program instead of the old one. This gave a new grating distribution (figure 4.4). Notice that there were a few times that the efficiencies suddenly dropped. The drops in efficiency seemingly happened when the center of the metaatoms moved from one side of the grating to the other in the optimization process. When investigating the issue, the drops in efficiency seem to have come from faulty calculations when one metaatom is outside the lattice.

In order to fix the faulty calculations, the metaatoms that happened to get outside the lattice got moved one into the lattice before simulating the structure instead of after simulating it in the optimization step. While investigating this, another problem with the optimizations came up, where the optimization sometimes started oscillating between equally optimal structures. That happened because only meta-gratings that had a lower efficiency was discarded. After changing the script such that equal efficiencies also got discarded and the faulty calculations fix gave new optimized efficiencies. See figure 4.5.

Using the phase mapping approach, 20 cylinders of TiO_2 were created with radii varying from 50 to 100 nm, and a height of 550 nm. These cylinders were then placed on a hexagonal grid with a 300 nm smallest distance between metaatoms such that the phase map of a lens was approximated by the metaatoms. This was done for the center of a lens with a focal length of 200 µm, and radius of 285 µm, where the center is the part where the deflection angle is smaller than 20°. for higher deflection angles, the optimized gratings (with efficiencies from figure 4.5) were used.

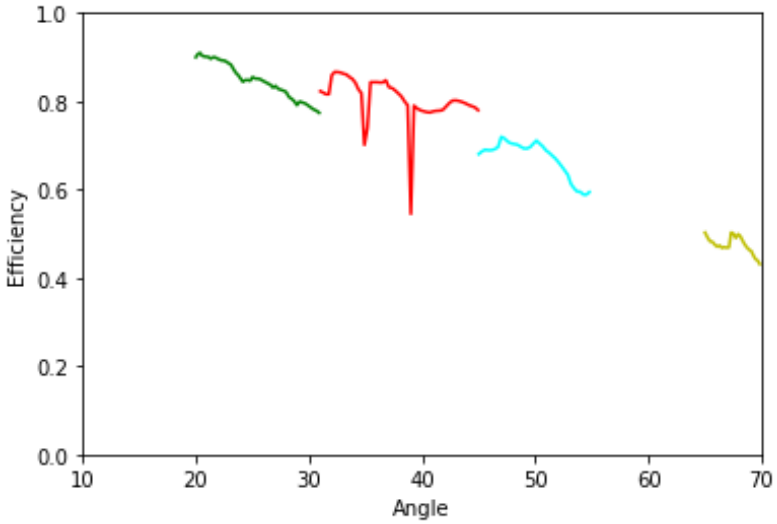

Figure 4.4: This is the efficiency obtained when the Python script used the new S^4 program instead of the old one, with the same starting conditions as in figure 4.1, but with 200 G-vectors instead of 100 for optimization. 300 G-vectors was used for the efficiency gathering. Notice that there are some sharp spikes where the efficiency drops significantly.

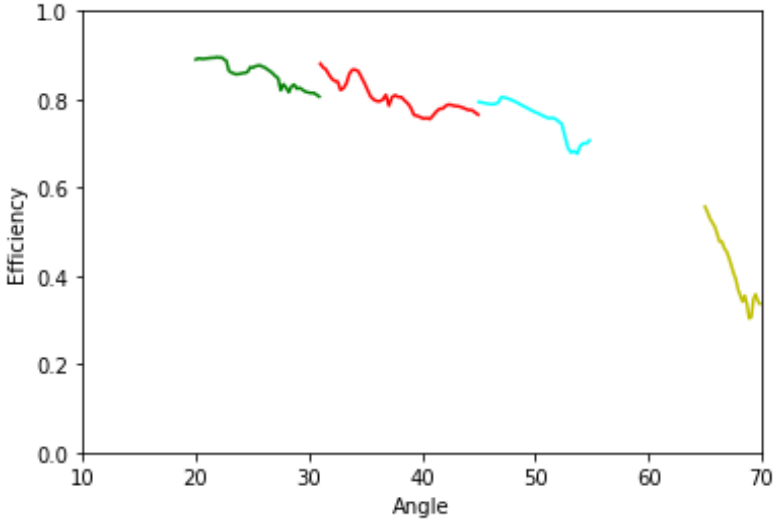

Figure 4.5: After some smaller changes in the optimization algorithm, such as moving the center-points of the ellipses before evaluating the efficiency during optimization seems to have made the less efficient gratings less common compared to in the case for figure 4.4. The rest of the differences could be explained through the optimization having random properties.

When an incoming x-polarized plane wave of wavelength 580 nm was applied from air, the nearfields from the lens are shown in figure 4.6.

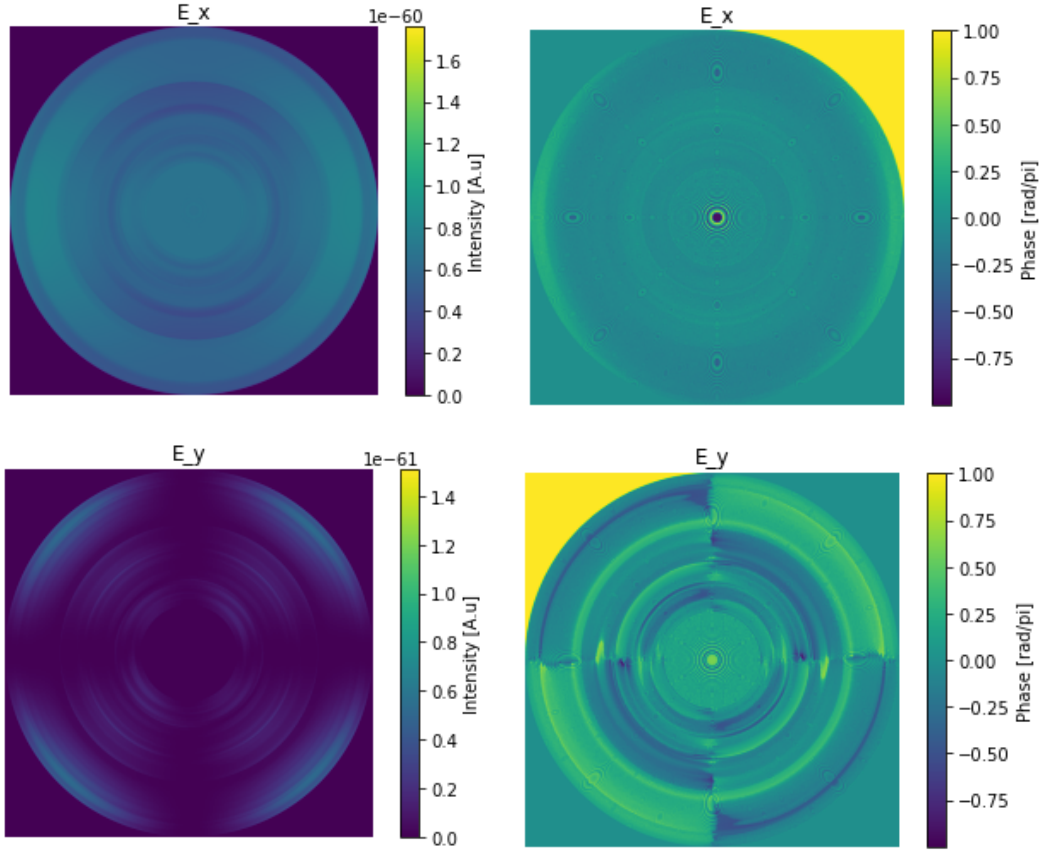

Figure 4.6: This figure show the simulated E-field immediately after the cylinders of the created lens when illuminated with x-polarized light ($z = 550$ nm, where the intersection between the substrate and metaatoms is at $z = 0$). The upper and lower figures show the x and y components of the field respectively, while the left figures and the right figures show the intensities of the field components ($|E_x|^2$ and $|E_y|^2$ respectively) in arbitrary units and the phase of the field components ($\arg(E_x)$ and $\arg(E_y)$ respectively) in radians/π. The yellow part in the upper corners of these figures should be ignored, since it is only a rounding error due to the field being close to 0 (since there is no metasurface there). One may also notice the ripples in the phases, which comes from the fact that we have a discrete structure.

4.2 Validating the S^4 program

Due to the randomness in the optimization process for the recreation of the lens, it is difficult to validate how well the S^4 program works. Therefore, a recreation of an already optimized cell would give a much better idea of how well the S^4 program holds up for the simulations made. After optimization with FDTD, Paniagua-Domínguez

et al. [2] optimized a grating designed to bend normally incident light with a wavelength of 715 nm at an angle of 82°.

The designed grating was made out of Si cylinders on top of a SiO_2 substrate in air, with a size of 721 nm×260 nm. The metaatoms had a height of 250 nm and the cylinders in the grating had diameters of 150 nm and 190 nm respectively with a gap between them of 50 nm. The recreated grating is found in figure 4.7.

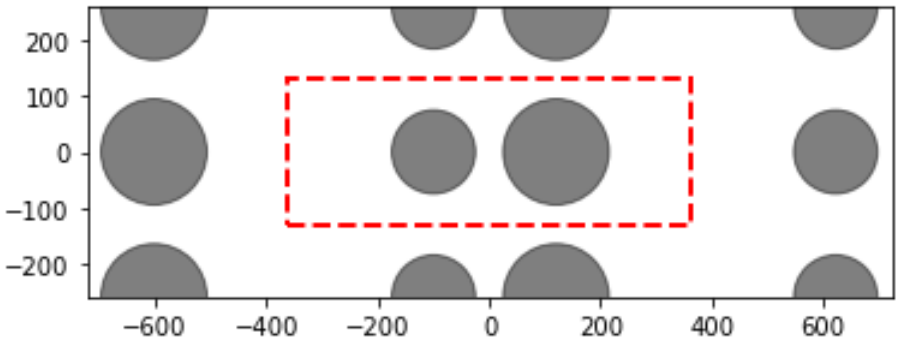

Figure 4.7: This was the grating used for validation. It was designed to look like an optimized grating for 82° deflection for normal incident light at a wavelength of 715 nm made by Paniagua-Domínguez et al. [2], using Si cylinders on a SiO_2 substrate in air.

Paniagua-Domínguez et al. simulated the efficiency of the diffraction orders depending on the wavelength and polarisation of light (see figure 2A and 2B in their article) [2]. Recreating those figures with the S^4 program gives figures 4.8 and 4.9. Comparing these figures with the ones simulated by Paniagua-Domínguez et al. shows some agreements on the overall shape of the curves, however it seems like the S^4 program gives a noisier data set from the simulations. In the upper range of the wavelengths shown in these figures ($\sim$ 650 nm and above), the agreement between the S^4 program and the FDTD approach seems to give fairly similar results.

When looking at the spectra in figures 4.9, there are a few sharp peaks that do not align with the FDTD simulated spectra that Paniagua-Domínguez et al. made. [2] Since these sudden shifts only happen in a short range of wavelengths, it is probable that these come from some division by almost zero problem when solving the eigenvalue equation (2.13). In order to make sure that the peaks did not happen through a bad choice of number of G-vectors (N_G), the efficiency spectra was simulated by sweeping over N_G from 100 G-vectors to 1500 G-vectors instead of wavelength (see figures 4.10 and 4.11). Since the Fourier-expansion should get more accurate when more terms are used, one may see that the simuluations get a fairly converged value after 400 G-vectors are used, and the added computation time after that is not really worth the extra accuracy. (Recall that the computation time scales as N^3, where N is the number of G-vectors)

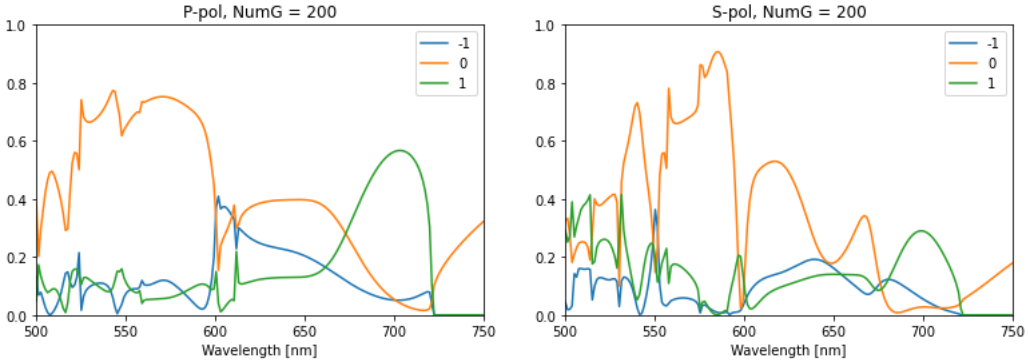

Figure 4.8: When using the S^4 program in order to simulate a wavelength spectrum for s- and p-polarized light with normal incidence to the grating shown in figure 4.7 with 200 G-vectors, these spectra are found. The p-polarisation is shown to the left and the s-polarisation is shown to the right. In each of the figures, the blue line gives deflection in the T_{-1} direction, the orange line is the spectrum in the T_0 direction and the green line is the spectrum in the T_{+1} direction. Notice that when the wavelength is larger than 721 nm, the wavelength of light is larger than the lattice constant, which means that the deflection angle would be $> 90°$, Therefore it is reasonable to see that the efficiency would be 0 there.

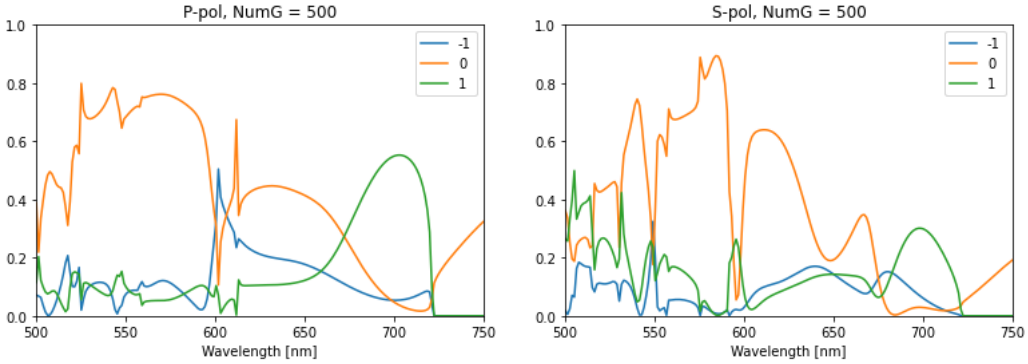

Figure 4.9: After capturing the wavelength spectrum in figure 4.8, some small peaks were visible. Since the number of G-vectors was not particularily large, another plot was made, but this time using 500 G-vectors instead. Suprisingly the odd peaks did not disappear, but instead got larger.

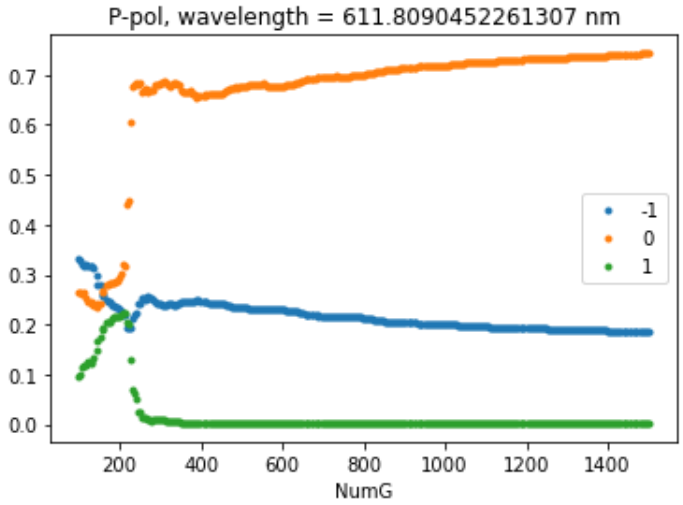

Figure 4.10: When comparing the figures made through the S^4 (figures 4.9 and 4.8) with the figures made through FDTD by Paniagua-Domínguez et al. [2] there are some short range large shifts in efficiency that do not agree with the FDTD method. One of these shifts can be found at a wavelength of $\lambda \approx 612$ nm when using p-polarization. By holding the wavelength constant, and sweeping through 300 numbers of G-vectors between 100 and 1500 ($100 \leq N_G \leq 1500$), one may see that the peaks do not go down with increasing N_G.

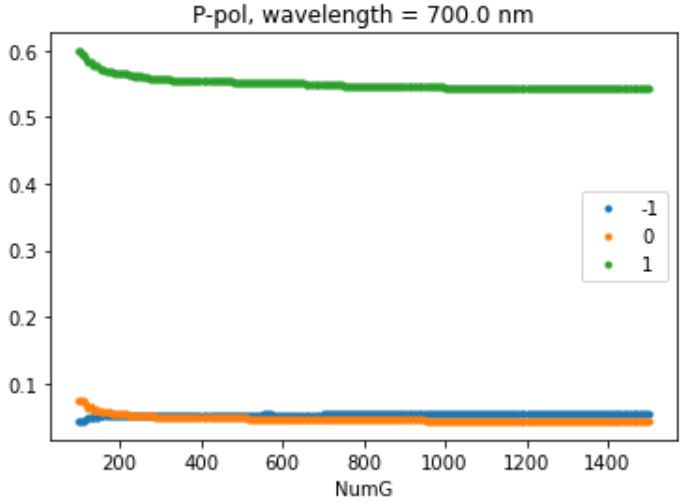

Figure 4.11: Doing the same sweep from figure 4.10, one may see that when we do not hit a peak, the efficiency does not depend strongly on the number of G-vectors (N_G), so we may say that these values are very converged for a low N_G. Note that as the efficiency was considered fairly converged at $N_G = 400$ in figure 4.10, the efficiencies may be fairly converged for $N_G = 250$ in this figure.

4.3 Optimized metasurface deflectors

After noticing that the efficiency is fairly converged for 400 G-vectors (Figures 4.10 and 4.11), three different deflection gratings were optimized. One grating for a deflection angle of 30° (figure 4.12), one for 45° (figure 4.13) and one for 60° (figure 4.14). When optimizing these gratings, the optimization method was slightly different to what was presented in 3.2. The optimization started with the rough and fine version of the first optimization step for 200 G-vectors. The optimization was then continued through the fine version again together with the second optimization step with 400 G-vectors instead.

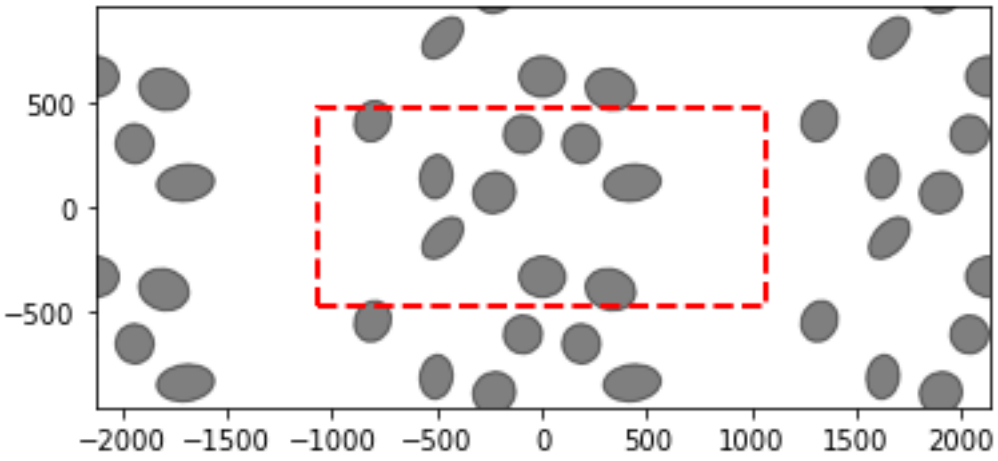

Figure 4.12: A grating optimized for 30° deflection in air, using 400 G-vectors with the S^4 program. According to the simulation, this grating should have approximately 89% efficiency in air when p-polarized light of wavelength $\lambda = 1064$ nm is used, the pilars are made of Si sitting on a substrate of SiO_2.

After a few simulations for both s- and p-polarized light only resulting in $< 50\%$ efficiency, it was decided to optimize for only one polarization of light in order to get a higher efficiency. The optimization was done for a few different periodicities in the y-direction and the grating with the best efficiency was chosen. As the metasurfaces was based on deflection gratings, the periodicity in the x-direction was chosen from the deflection angle.

The optimized gratings (figures 4.12, 4.13 and 4.14) were manufactured through etching of a stacked slab containing 490 nm Si on top of a substrate of SiO_2. After creation, the metasurfaces were sputtered with gold, in order to make it possible to conduct electrons through the surface. This was done in order to make it possible to do the SEM images seen in figures 4.15, 4.16 and 4.17. Everything from manufacturing the optimized gratings to taking the SEM images was done by Mahdi Shanei.

When doing the experiments, the beam power was measured by letting the light go through the SiO_2 layer without a metasurface, which gave both the zero order

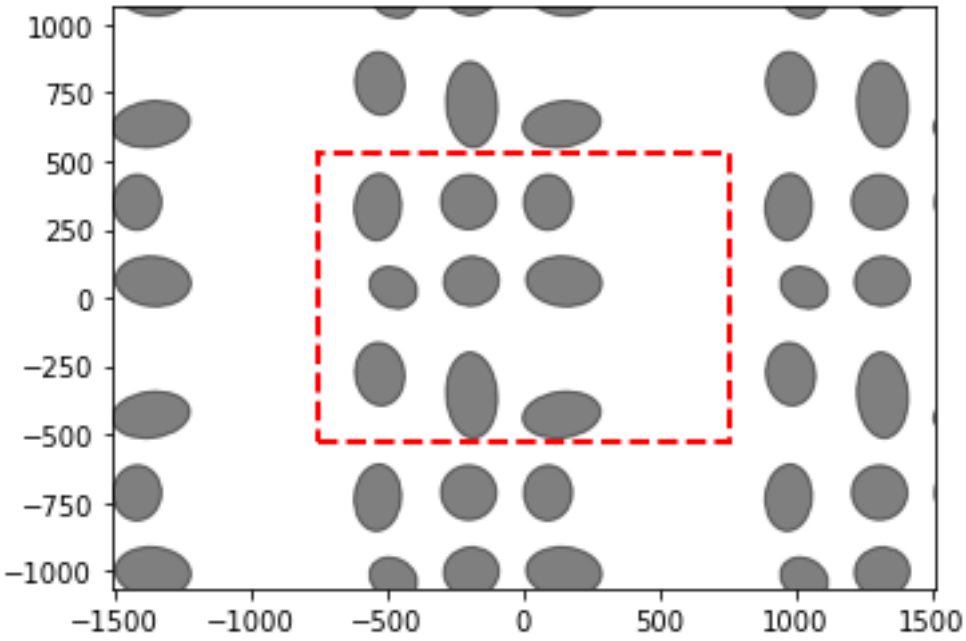

Figure 4.13: A grating optimized for 45° deflection, using 400 G-vectors with the S^4 program. According to simulation, this grating should have approximately 91% efficiency in air when p-polarized light of wavelength $\lambda = 1064$ nm is used, the pilars are made of Si sitting on a substrate of SiO_2.

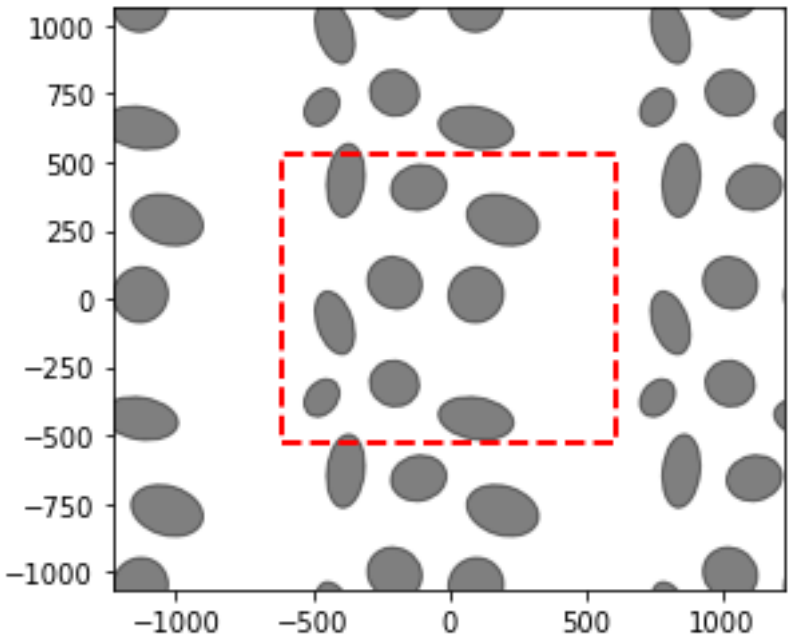

Figure 4.14: A grating optimized for 60° deflection, using 400 G-vectors with the S^4 program. According to simulation, this grating should have approximately 83% efficiency in air when p-polarized light of wavelength $\lambda = 1064$ nm is used, the pilars are made of Si sitting on a substrate of SiO_2.

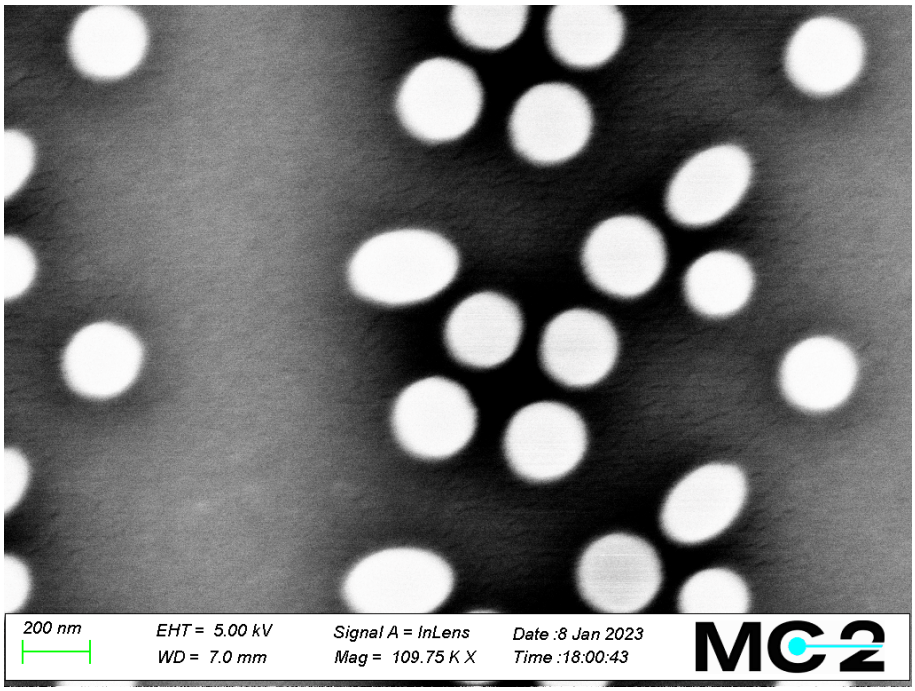

Figure 4.15: A SEM-image of the etched grating, using figure 4.12 as a map. Notice that the grating shown here is upside down. This photo was taken by Mahdi Shanei.

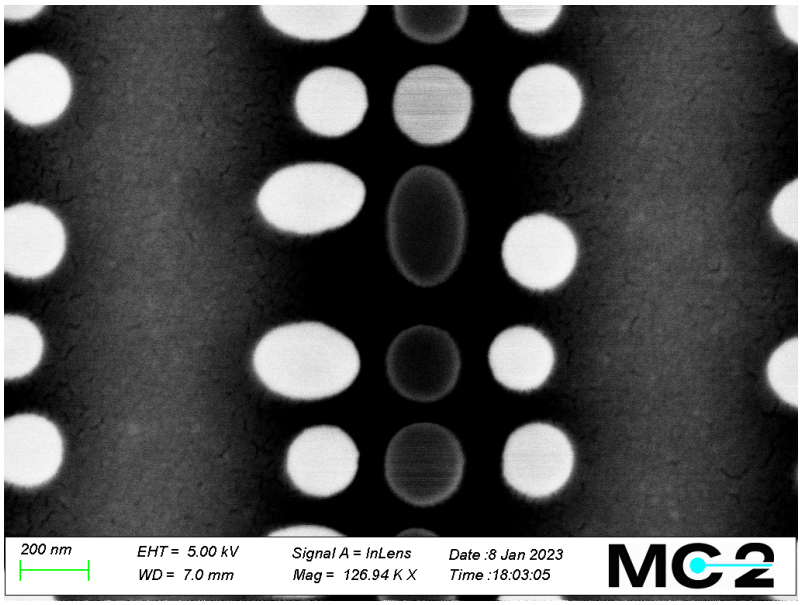

Figure 4.16: A SEM-image of the etched grating, using figure 4.13 as a map. Notice that the grating shown here is upside down. The metaatoms in the middle row are darker since they did not get as covered as the outer metaatoms from the gold sputtering used in order to get the SEM images. This photo was taken by Mahdi Shanei

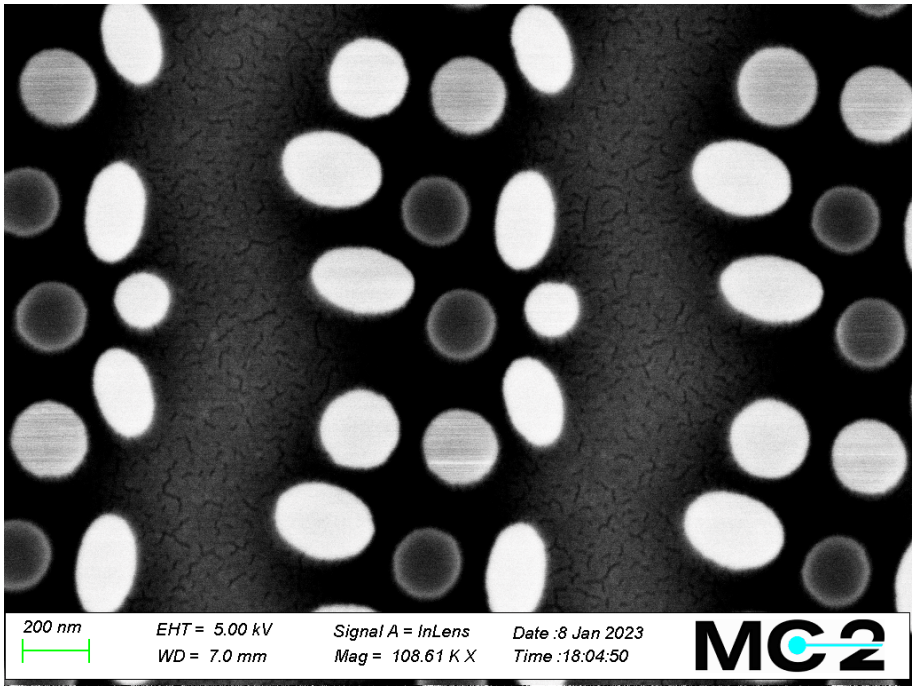

Figure 4.17: A SEM-image of the etched grating, using figure 4.14 as a map. Notice that the grating shown here is upside down. The metaatoms in the middle row are darker since they did not get as covered as the outer metaatoms from the gold sputtering used in order to get the SEM images. This photo was taken by Mahdi Shanei

Table 4.1: Results from the experimental measurements in oil is shown in this table. The first column states the deflection angle in air (in oil) of the grating. When using a specific grating, the second column notes the distance from the zero order peak to the +1 order peak. This gives the incoming angle to the camera lens to be θ/R, with an efficiency, which could be compared to the simulated efficiency, where the simulation of the efficiencies were done again, but this time the simulations were for the gratings in oil ($n = 1.51$) rather than in air ($n = 1$).

Grating angle (θ)	Distance [µm]	θ/R	Efficiency	S^4 efficiency
30° (19.34°)	331.48	0.38°	29.0%	37.1%
45° (27.91°)	469.66	0.54°	55.5%	59.4%
60° (35.00°)	573.21	0.66°	49.5%	49.5%

position of the beam, and the intensity for 100% efficiency. One thing to note with this approach is that some energy is lost by the wave reflecting from the glass to air when no metasurface is present, giving the possibility for measured efficiencies above 100%. By doing a simulation without a metasurface, the lost intensity was at most 0.01%, meaning that the loss is negligible, and the efficiencies should give similar results to the simulations. After doing the experimental measurements on the gratings, the pictures from the Fourier plane camera were saved as bitmaps, imported in Python and analyzed for each peak.

The distance between the found peak and the zero order peak (Δx) can be used in order to find the deflection angle through $\Delta x = f \tan(\theta/R)$. Using this fact, it is possible to find the value for θ/R. The intensity of each peak was also calculated through summation of the intensity values for the pixels around the peak pixel in the Fourier plane image until the intensity had dropped below $1/e^2$ times the maximum peak value. Calculations of intensity were done through dividing the number of photons captured during exposure of the camera by the exposure time. In order to calculate the efficiency, the reference intensity was measured as the zero order deflection without a metasurface with an exposure time of around 5ms. The efficiency was then calculated as the fraction between the intensity for the +1 order peak and the reference intensity. This gives the results as shown in table 4.1.

By looking at table 4.1, one may note that for the deflection angles θ to be consistent with the measured angles θ/R, the reduction coefficient R cannot be constant ($R_1 = 19.34/0.38 \approx 51$, while $R_3 = 35.00/0.66 \approx 53$, meaning $R_1 \neq R_3$). When measuring the grating periodicities from the SEM figures (figures 4.15, 4.16 and 4.17), the measured periodicities align well with the simulated periodicities. By the grating equation, $P = \lambda/(n \sin\theta)$, the periodicity P must correspond to the deflection angle θ, which in turn means that the reduction coefficient R depends on deflection angle.

When instead looking at the efficiencies, for the first angle ($\theta = 19.34°$), the experimental efficiency (29%) was fairly far from the simulated efficiency (37.1%). This is especially true when comparing to the other gratings, which are closer to the simulation efficiencies. One may note that this could mean either that the S^4 program got

a bad value when simulating that grating, or that the fabricated metasurface had some small defects in the structure such that it is different to the designed structure. More data would however be needed in order to make any lasting statements, but the fact that the metaatoms were not placed in a structured order might be a key to understanding why that is.

Going over to the other gratings, one may see that the metaatoms are more aligned in a somewhat square matrix, which could have made the fabrication more precise. If these gratings also would be less prone to the small changes from the fabrication, their efficiencies should be closer to the simulated ones, which is also what is seen here. However, more studies would be necessary to make a concluding claim in this area.

5

Conclusions

In order to create metasurfaces with 2π phase-shifts the S^4 program was used, based on an article by J. Byrnes et al. [1] that had used that program in order to optimize a lens. By using the same version of the S^4 program as J. Byrnes et al. it was possible to recreate a similarly efficient lens using their Python scripts [20]. The version they had used to optimize their structure has since been updated. By updating the program, the efficiencies of the gratings had changed, which can be seen in the change from figure 4.1 to figure 4.3. By making a new optimization from the start using the same technique, but with some minor adjustments in the optimizations resulted in figure 4.5, which still is roughly the same efficiencies that Byrnes et al. [1] showed.

Later, the method was tested based on an already optimized grating that Paniagua-Domínguez et al. [2] had previously made, and was compared to their results. Figure 4.9 show similar results to their FDTD images, however the S^4 program seem to have many more large peaks that were not visible in their FDTD approach. One could note however that what was seen experimentally seem to agree in a similar degree when using the RCWA method and the FDTD method when simulating the same thing.

For some original work, a few gratings were optimized with the same optimization technique that was used to optimize the gratings in the lens (see figures 4.12, 4.13 and 4.14). In order to see how well these gratings performed, they were fabricated and compared with the simulated values, and the gratings with the larger deflection angle compared well, while the grating with the lowest deflection angle did not compare well at all (see table 4.1). One factor that stood out specifically with the grating in figure 4.12 was that the metaatoms were fairly spread out over the entire grating rather than placed in somewhat of a lattice, which might have been a factor to why the grating did not get the same results that the S^4 program predicted.

Going back to the aim of the thesis, namely to see how well the RCWA method works through the S^4 program. It has been shown through figures 4.8 and 4.9 that the S^4 program can calculate efficiencies with similar accuracy to the FDTD method for large wavelengths. It has also been shown in table 4.1 that the program can calculate efficiencies similar to what was seen in experiments for a few deflection angles. The S^4 program can therefore be recommended for use to optimize gratings.

However as the simulations got less accurate for lower wavelengths and deflection angles, another approach could be considered on the optimized structure before trusting the S^4 simulations at those points.

5.1 Future work

In this work, the S^4 program was used in order to simulate gratings. By simulating these, they could be optimized and fabricated to compare with the simulated gratings. As stated, the experimental value for the grating in figure 4.12 was not as expected. A study on if that was because of an inaccuracy of the S^4 program or if it was because of the gratings being less evenly distributed would be instructive. This could lead to better knowledge in estimation of fabrication errors of metasurface gratings based on how the grating looks like.

Another interesting, but short, project would be to investigate when the phase map could be considered linear in practice. We know from the theory that the phase map could be considered linear when $|\nabla^2\varphi| \ll |\nabla\varphi|^2$. It would be interesting to experimentally verify when this actually holds true. This could later be used in a project that could simulate a holographic metasurface, in order to introduce metagratings there.

As this thesis did not look at the absorption coefficients of the materials, some errors might be at hand for smaller wavelengths due to that. It would therefore be interesting to look at complex permittivities, which S^4 can handle. The results also only came from using a scalar permittivity, however some materials can be described with tensoral permittivities instead. It would also be interesting to see if those materials could be made into metaatoms, and could be simulated in a similar manner.

Bibliography

[1] S. J. Byrnes, A. Lenef, F. Aieta, and F. Capasso, "Designing large, high-efficiency, high-numerical-aperture, transmissive meta-lenses for visible light," *Opt. Express*, vol. 24, no. 5, pp. 5110–5124, Mar 2016. [Online]. Accessible: https://opg.optica.org/oe/abstract.cfm?URI=oe-24-5-5110

[2] R. Paniagua-Domínguez *et al.*, "A metalens with a near-unity numerical aperture," *Nano Letters*, vol. 18, no. 3, pp. 2124–2132, 2018, pMID: 29485885. [Online]. Accessible: https://doi.org/10.1021/acs.nanolett.8b00368

[3] J. Engelberg and U. Levy, "The advantages of metalenses over diffractive lenses," *Nature Communications*, vol. 11, no. 1, p. 1991, Apr 2020. [Online]. Accessible: https://doi.org/10.1038/s41467-020-15972-9

[4] N. Yu *et al.*, "Light propagation with phase discontinuities: Generalized laws of reflection and refraction," *Science*, vol. 334, no. 6054, pp. 333–337, 2011. [Online]. Accessible: https://www.science.org/doi/abs/10.1126/science.1210713

[5] S.-W. Moon *et al.*, "Tutorial on metalenses for advanced flat optics: Design, fabrication, and critical considerations," *Journal of Applied Physics*, vol. 131, no. 9, p. 091101, 2022. [Online]. Accessible: https://doi.org/10.1063/5.0078804

[6] T. Shi *et al.*, "All-dielectric kissing-dimer metagratings for asymmetric high diffraction," *Advanced Optical Materials*, vol. 7, no. 24, p. 1901389, 2019. [Online]. Accessible: https://onlinelibrary.wiley.com/doi/abs/10.1002/adom.201901389

[7] H. Ren, X. Fang, J. Jang, J. Bürger, J. Rho, and S. A. Maier, "Complex-amplitude metasurface-based orbital angular momentum holography in momentum space," *Nature Nanotechnology*, vol. 15, no. 11, pp. 948–955, Nov 2020. [Online]. Accessible: https://doi.org/10.1038/s41565-020-0768-4

[8] Y. Zhang *et al.*, "Electrically reconfigurable non-volatile metasurface using low-loss optical phase-change material," *Nature Nanotechnology*, vol. 16, no. 6, pp. 661–666, Jun 2021. [Online]. Accessible: https://doi.org/10.1038/s41565-021-00881-9

[9] H. T. Jang and J. C. Yi, "Comparison of rigorous coupled-wave analysis and finite difference time domain method on dielectric gratings," in *2021 IEEE Region 10 Symposium (TENSYMP)*, 2021, pp. 1–4.

[10] V. Liu and S. Fan, "S^4 : A free electromagnetic solver for layered periodic structures," *Computer Physics Communications*, vol. 183, no. 10, pp. 2233–2244, 2012. [Online]. Accessible: https://www.sciencedirect.com/science/article/pii/S0010465512001658

[11] M. Kang, Y. Ra'di, D. Farfan, and A. Alù, "Efficient focusing with large numerical aperture using a hybrid metalens," *Phys. Rev. Applied*, vol. 13, p. 044016, Apr 2020. [Online]. Accessible: https://link.aps.org/doi/10.1103/PhysRevApplied.13.044016

[12] D. King, K. Hettak, R. Chaharmir, J. Ethier, and S. Gupta, "Phase-only synthesis methods for general beam-forming reflective metasurfaces," in *2020 IEEE International Symposium on Antennas and Propagation and North American Radio Science Meeting*, 2020, pp. 917–918.

[13] H. Ahmed *et al.*, "Optical metasurfaces for generating and manipulating optical vortex beams," *Nanophotonics*, vol. 11, no. 5, pp. 941–956, 2022. [Online]. Accessible: https://doi.org/10.1515/nanoph-2021-0746

[14] H. Toba, H. Takagi, M. Ohashi, K. Otaki, and Y. Takigawa, "Influence on wide-angle doublet metalenses due to different types of all-dielectric metasurfaces," *Appl. Opt.*, vol. 61, no. 2, pp. 597–606, Jan 2022. [Online]. Accessible: https://opg.optica.org/ao/abstract.cfm?URI=ao-61-2-597

[15] D. Li and Y. Li, "An aberration-corrected single layer metasurface with large field of view," *Optics Communications*, vol. 530, p. 129195, 2023. [Online]. Accessible: https://www.sciencedirect.com/science/article/pii/S0030401822008422

[16] S. So, J. Mun, J. Park, and J. Rho, "Revisiting the design strategies for metasurfaces: Fundamental physics, optimization, and beyond," *Advanced Materials*, vol. n/a, no. n/a, p. 2206399, Sep 2022. [Online]. Accessible: https://doi.org/10.1002/adma.202206399

[17] J. Zhang *et al.*, "Metalenses with polarization-insensitive adaptive nano-antennas," *Laser & Photonics Reviews*, vol. 16, no. 9, p. 2200268, 2022. [Online]. Accessible: https://onlinelibrary.wiley.com/doi/abs/10.1002/lpor.202200268

[18] J. J. Sakurai and J. Napolitano, *Modern Quantum Mechanics*, 2nd ed. Cambridge University Press, 2017, ch. 2, pp. 110–112.

[19] V. Liu. (2015) S^4 documentation. Available 2022-09-27. [Online]. Accessible: https://github.com/victorliu/S4/pull/25/files

[20] S. J. Byrnes. (2017) Metalens design and simulation code. Available 2022-09-27. [Online]. Accessible: https://github.com/sbyrnes321/metalens

[21] V. Liu. (2018) S^4 program code. Available 2022-09-27. [Online]. Accessible: https://github.com/victorliu/S4

A

Grating information

For recreation purposes, the structures that were optimized is shown below. Note that the xyrra list is a list of all metaatoms used, containing the center position (x, y), the elliptical radii used (r_x, r_y), and the angle that the metaatom is rotated around its center a.

A.1 Starting gratings for the lens

When optimizing the structure of the lens, the xyrra lists used for starting the optimization was different depending on the starting angle. The optimized grating collections can be seen in figure 4.5. The first grating collection (20° to 31°) used five elliptical cylinders, and the starting grating before any optimizations had a xyrra list as follows.

x [nm]	y [nm]	r_x [nm]	r_y [nm]	a [°]
−600	0	100	100	0
−300	175	100	100	0
0	0	100	100	0
300	−175	80	80	0
600	0	60	60	0

The second grating (31° to 45°) used four elliptical cylinders instead. This led to the starting xyrra list instead looking like what is seen in the table bellow.

x [nm]	y [nm]	r_x [nm]	r_y [nm]	a [°]
−550	0	100	100	0
−260	175	100	100	0
0	0	80	80	0
260	−175	60	60	0

The third grating collection (45° to 55°) only used two cylinders, which used a starting grating with a xyrra list of

x [nm]	y [nm]	r_x [nm]	r_y [nm]	a [°]
−200	−100	100	70	0
100	100	100	70	0

The last deflection grating (65° to 70°) also only used two cylinders, using a starting grating with a xyrra list that looks like

x [nm]	y [nm]	r_x [nm]	r_y [nm]	a [°]
−350	100	100	100	0
0	−100	100	100	0

A.2 Validation grating

For the grating, see figure 4.7. The horizontal periodicity is defined from the deflection angle of $\theta = 82°$, given a design wavelength of $\lambda = 715$ nm (which gives a periodicity of $P_x \approx 721$ nm), the vertical periodicity is 260 nm and the height of the pillars are 250 nm. The xyrra list of the cylinders can be seen in the table below.

x [nm]	y [nm]	r_x [nm]	r_y [nm]	a [°]
−100	0	75	75	0
120	0	95	95	0

A.3 Optimized deflectors

All of the deflectors (see figures 4.12, 4.13 and 4.14) used have the same height of the cylinders of 490 nm, and had the same starting xyrra list before optimization seen below. These gratings were all optimized for a design wavelength of $\lambda = 1064$ nm, their periodicities will be stated later.

x [nm]	y [nm]	r_x [nm]	r_y [nm]	a [°]
−600	−300	90	90	0
−600	0	90	90	0
−600	300	90	90	0
−200	−300	90	90	0
−200	0	90	90	0
−200	300	90	90	0
200	−300	90	90	0
200	0	90	90	0
200	300	90	90	0

For the 30° deflector (figure 4.12), the grating used had a periodicity in the vertical direction of 950 nm, and in the horizontal direction, the periodicity used was approximately 2128 nm, based on the 30° deflection. The xyrra list is written in the table below.

x [nm]	y [nm]	r_x [nm]	r_y [nm]	a [°]
−472.64	−149.96	71.15	119.24	−44.21
−503.51	143.62	77.38	104.48	−7.25
−806.25	407.78	99.06	84.69	66.01
1.78	−331.02	110.54	96.54	−1.43
−227.48	68.53	96.42	102.96	−55.58
−90.78	345.14	91.49	90.67	16.23
326.78	−391.97	120.52	97.13	−15.82
429.77	114.96	136.87	86.75	6.54
187.81	300.80	90.36	93.78	8.91

For the 45° deflector (figure 4.13), the grating used had a periodicity in the vertical direction of 1064 nm, and in the horizontal direction, the periodicity used was approximately 1505 nm, based on the 45° deflection. The xyrra list is written in the table below.

x [nm]	y [nm]	r_x [nm]	r_y [nm]	a [°]
−525.41	−279.84	90.08	115.80	7.22
−475.98	36.46	91.27	72.66	−27.18
−532.91	331.92	85.43	122.56	−4.40
−188.79	−356.98	93.18	157.25	3.55
−190.40	60.08	101.05	90.52	6.41
−200.00	350.03	102.02	99.93	−13.51
140.94	−429.07	143.06	83.85	7.17
149.09	59.32	138.46	91.34	−4.58
90.62	348.86	88.65	101.17	−1.94

For the 60° deflector (figure 4.14), the grating used had a periodicity in the vertical direction of 1064 nm, and in the horizontal direction, the periodicity used was approximately 1229 nm, based on the 60° deflection. The xyrra list is written in the table below.

x [nm]	y [nm]	r_x [nm]	r_y [nm]	a [°]
−465.86	−363.44	56.57	74.75	−38.23
−418.38	−88.50	64.88	119.21	18.37
−378.31	432.81	68.03	134.28	−6.03
−200.12	−311.07	90.65	83.34	−17.04
−199.25	57.70	101.70	92.94	−31.93
−111.14	406.83	101.92	82.52	11.56
98.71	−438.84	138.21	76.43	−9.07
98.49	14.02	99.52	102.40	−38.25
196.45	288.04	133.99	89.39	−16.47

A.3.1 Another optimized deflector

When trying to do a small simulation after the gratings was manufactured, another optimization was accidentally run simultaneously, and happened upon a very effi-

cient (97%) grating for deflecting p-polarized light at an angle of 60° (see figure A.1). The horizontal periodicity shown is again approximately 1229 nm, and the vertical periodicity is 950 nm.

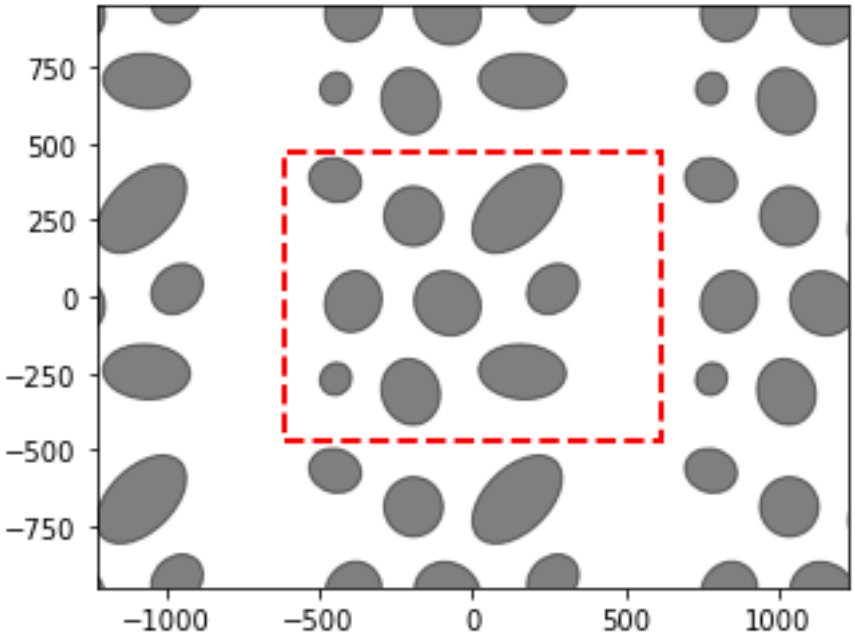

Figure A.1: Efficient grating

x [nm]	y [nm]	r_x [nm]	r_y [nm]	a [°]
−446.38	−269.22	50.40	54.13	−32.93
−388.84	−16.02	101.95	90.89	64.48
−448.18	381.09	86.08	71.13	−16.48
−201.23	−311.36	94.71	109.05	17.14
−80.79	−21.94	112.00	101.75	−34.21
−192.04	263.00	96.00	97.35	2.11
163.86	−245.85	142.57	89.62	−3.62
263.75	24.91	74.76	91.36	−48.27
147.05	287.01	176.96	104.50	44.08

DEPARTMENT OF PHYSICS
CHALMERS UNIVERSITY OF TECHNOLOGY
Gothenburg, Sweden
www.chalmers.se

CHALMERS
UNIVERSITY OF TECHNOLOGY